



Supplementary Materials for

Cryo-EM structure of a dimeric B-Raf:14-3-3 complex reveals asymmetry in the active sites of B-Raf kinases

Authors:

Yasushi Kondo^{1,2,†}, Jana Ognjenović^{3,†,‡}, Saikat Banerjee⁴, Deepti Karandur^{1,2,5}, Alan Merk^{3,‡},
Kayla Kulhanek⁴, Kathryn Wong^{1,2,§}, Jeroen P. Roose⁴, Sriram Subramaniam^{6,*}, John
Kuriyan^{1,2,5,7,8*}

Correspondence to: kuriyan@berkeley.edu, Sriram.Subramaniam@ubc.ca

This PDF file includes:

Materials and Methods
Figs. S1 to S17
Tables S1 to S2
References (37-62)

Materials and Methods

Protein Preparation

Production of full-length B-Raf using intein chemistry

5 In order to overcome solubility and proteolysis problems during expression and purification, we split human B-Raf (gene id: 673) into two fragments, each fused to one half of a split intein (37), expressed and purified them separately and joined them together by the intein reaction. After screening multiple constructs, we chose to insert the split intein between residues Asn³⁷² and Thr³⁷³, located in the middle of a long linker between the N-terminal and the C-terminal segments of B-Raf. The N-terminal fragment was purified from bacterial cells, but the C-terminal fragment required expression in insect Sf9 cells. The two fragments were ligated using intein chemistry (37) and the full-length protein was further purified (Fig. S16). The intein reaction introduces two mutations in the linker (T373C and I374M) required for efficient intein reaction, but otherwise the final product is full-length human B-Raf.

10 The B-Raf N-terminal fragment (1-372) followed by the consensus split intein CfaN sequence (37) was cloned into the 2C-T vector (Addgene plasmid # 29706). The expression vector fuses six histidine residues, maltose binding protein, and a TEV protease cleavage site to the N-terminal end of B-Raf. The B-Raf C-terminal expression construct adds six histidine residues, glutathione S-transferase, a TEV protease cleavage site, and the split intein NpuC sequence to the N-terminal end of the B-Raf C-terminal fragment (373-766), with two mutations, T373C and I374M. This construct was inserted into the pFastBac Dual vector (Thermo Fisher). The human CDC37 gene (Addgene plasmid # 40368) was cloned into the second expression cassette of the vector to enhance B-Raf expression levels (20).

20 The B-Raf N-terminal fragment was expressed in *E. coli* Rosetta2 (DE3) cells (Novagen). Protein expression was induced at an optical density at 600 nm (OD₆₀₀) of 0.4, and cultured overnight at 15°C before harvesting the cells by centrifugation. The cell pellet was suspended in Ni-A buffer (20 mM Tris pH 8.0, 500 mM NaCl, 500 mM Urea, 0.5 mM TCEP), and the cells were lysed by sonication. Cell debris was removed by ultracentrifugation. The supernatant was applied to a HisTrap column (GE Healthcare). The column was washed with Ni-A2 buffer (20 mM Tris pH 8.0, 100 mM NaCl, 0.5 mM TCEP) and the protein was eluted by Ni-A2 buffer supplemented with 400 mM imidazole. The eluate was further fractionated on a HiTrap Q column (GE Healthcare) equilibrated with Q-A buffer (20 mM Tris pH 8.0, 50 mM NaCl, 0.5 mM TCEP), using a linear gradient of NaCl (0.05 M – 1 M). The protein was concentrated by ultrafiltration using Amicon Ultra with a 50 kDa molecular-cutoff filter and further purified over an S 200 size-exclusion chromatography column (GE Healthcare) that was pre-equilibrated with SEC buffer (20 mM Tris pH 8.0, 300 mM NaCl, 0.5 mM TCEP). The N-terminal tag was not cleaved during the purification in order to keep the protein soluble (38). The purified protein was concentrated to ~100 µM, based on UV absorbance at 280 nm, supplemented with 40% glycerol, and stored at -20°C.

35 The B-Raf C-terminal fragment was expressed in insect Sf9 cells. Sf9 cells were infected with baculovirus with the expression cassettes and grown for two days and harvested by centrifugation. The cell pellet was suspended in Ni-A buffer supplemented with complete protease inhibitor (Roche), and the cells were lysed by sonication. The supernatant was collected after ultracentrifugation and applied to a HisTrap column. The protein was eluted with 400 mM imidazole. Fresh complete protease inhibitor was added to the eluted protein, and the fusion tag was cleaved off by overnight incubation with TEV protease, while the sample was dialyzed against

Ni-A3 buffer (20 mM Tris pH 8.0, 300 mM NaCl, 5 mM β -mercaptoethanol). The dialyzed sample was reapplied to the HisTrap column and the flow-through was collected. The protein was concentrated by ultrafiltration, using an Amicon Ultra 30 kDa molecular-cutoff filter and applied to an S 200 column equilibrated with SEC buffer. The protein was concentrated to ~ 80 μ M, based on UV absorbance at 280 nm, and flash-frozen in liquid nitrogen and stored at -80°C .

The C-terminal fragment copurified with two proteins that were confirmed by mass-spectrometry to be the ϵ and ζ isoforms of insect cell 14-3-3. Mass-spectrometry also identified phosphorylation at sites known to be key for Raf activation (*I*), including at the N-terminal acidic (NtA) motif, the activation loop, as well as the carboxy terminal 14-3-3 binding site. The N-terminal fragment was produced in bacterial cells and is therefore not expected to be phosphorylated. The lack of phosphorylation at Ser³⁶⁵ in purified full-length B-Raf, the product of intein reaction, was confirmed by western blot using phospho-C-Raf (Ser²⁵⁹) antibody (Cell Signaling Technology), which also detects B-Raf Ser³⁶⁵ phosphorylation (39) (Fig. S16B). The accessibility of Ser³⁶⁵ in the purified B-Raf and the efficiency of the antibody was confirmed by incubating B-Raf with PKA (New England Biolabs) and ATP (Fig. S16B).

The intein reaction was set up by mixing the purified N- and C-terminal fragments of B-Raf in an equimolar ratio in intein buffer (20 mM Na-Hepes pH 7.0, 500 mM NaCl, 1 M urea, 3 mM MgCl₂, 10 mM TCEP). TEV protease was added to the intein reaction and incubated at 4°C overnight. The sample was applied to a Superose 6 size-exclusion chromatography column (GE Healthcare) with S6 buffer (20 mM Tris pH 8.0, 150 mM NaCl, 0.5 mM TCEP). Collected fractions were concentrated by ultrafiltration using Amicon Ultra 50 kDa molecular-cutoff centrifugal filter units.

We confirmed that the purified full-length B-Raf:14-3-3 complex has enzymatic activity and that it can phosphorylate MEK1, purified as described below (Fig. S1). We also prepared samples of the C-terminal fragment alone (residues 433 to 766), but this did not result in suitable cryo-EM samples due to increased aggregation of the protein.

Cloning, expression and purification of FLAG-tagged B-Raf from HEK293T cells

The human B-Raf variants, B-Raf-WT (residues 1-766), B-Raf- Δ DTS (1-735), B-Raf- Δ N (433-766), and B-Raf- Δ N Δ DTS (433-735), were cloned into the peGFP-N1 vector (Clontech) to generate N-terminally FLAG-tagged B-Raf proteins. An EGFP tag in the plasmid backbone was removed by the cloning procedure. HEK293T cells were transfected with the plasmids using calcium phosphate. The cells were harvested from culture dishes 24 hrs after transfection and suspended with FLAG-A buffer (100 mM Tris pH 8.0, 500 mM NaCl, 500 mM urea, 1 mM MgCl₂). The cell suspensions were supplemented with complete protease inhibitor, lysed by sonication, and cleared by centrifugation. The supernatant was incubated with anti-FLAG M2 affinity gel (Sigma) for at least 2 hrs at 4°C and applied to a Micro Bio-Spin column. The resin was washed with FLAG-A buffer followed by a wash with FLAG-A2 buffer (20 mM Tris pH8.0, 150 mM NaCl, 1 mM MgCl₂). FLAG-tagged B-Raf protein was eluted with FLAG-A2 buffer supplemented with 150 μ g/mL FLAG peptide and complete protease inhibitor. Protein quantity was estimated by the band intensities on a SDS-PAGE gel stained with Coomassie Brilliant Blue.

Cloning, expression and purification of MEK1

The human MEK1 gene was cloned from an MBP-MEK1 plasmid (Addgene plasmid # 68300) into the pET28a vector to generate a construct spanning residues 37 to 393 of MEK1, with a C-terminal hexa-histidine tag. The catalytic activity of MEK1 was disrupted by mutation (D190N). MEK1 protein expression was induced at OD₆₀₀ 0.4 in *E. coli* Rosetta2 (DE3) cells and cultured overnight at 18°C before harvesting. The cells were lysed and cleared by centrifugation as for the B-Raf N-terminal fragment preparation. The supernatant was applied to a HisTrap column and eluted with Ni-A buffer supplemented with 400 mM imidazole. The elution fraction was concentrated by ultrafiltration using Amicon Ultra 30 kDa molecular-cutoff centrifugal filter units and applied to an S 75 size-exclusion chromatography column equilibrated with SEC buffer. MEK1 protein fractions were collected and concentrated to 500 μM based on UV absorbance at 280 nm. The protein was flash-frozen by liquid nitrogen and stored at -80°C.

Cryo-EM grid preparation and data collection

To prepare samples for cryo-EM, 3 μL of protein sample at a concentration of ~0.2 mg/mL was applied to previously plasma-cleaned Quantifoil Cu R 1.2/1.3 200 mesh holey carbon grids (Electron Microscopy Sciences Q250CR-06). Grids were plasma cleaned using the Solarus 950 plasma cleaning system (Gatan) for 15s at 50 Watts using the hydrogen/oxygen plasma. Grids were blotted using Leica EM GP automatic plunge freezer (Leica Microsystems INC) for 8 s at +5°C and 95% humidity followed by plunge-freezing into liquid ethane cooled at ~ -184°C by liquid nitrogen. Vitrified grids were imaged using a Titan Krios transmission electron microscope (Thermo Fisher Scientific) equipped with a K2 Summit direct electron detector (Gatan) and GIF Quantum Energy Filter with a slit width of 20 eV operated at 300 keV at National Cryo-electron Microscopy Facility (NCEF). All cryo-EM movies were acquired at a nominal magnification of 130,000x, corresponding to a super-resolution pixel size of 0.532 Å, using Latitude (Gatan) data collection software. A total of 2,991 micrographs were collected as a 40-frame movie with total accumulated dose of 50 e-/Å² per micrograph over two separate data collection sessions, with applied defocus values between -1.25 and -2.5 μm.

Image processing

All movies from two separate data collection sessions were processed using RELION 3.0 (40). Images were motion-corrected and dose-weighted using MotionCor2 (41). Contrast transfer function (CTF) estimation was performed using CTFFIND4 (42). About 1.3 million particles were picked by RELION 3.0 from each dataset. Particles from good 2D classes from the two datasets were selected and joined (1.5 million particles in total) for 3D classification using an initial model generated from a subset of particles. The 3D class with the highest resolution was selected and further refined. The density of 14-3-3 was subtracted from each particle image and the particles resulted from the subtraction were further classified using the kinase domain region only by 3D classification without image alignment to overcome apparent flexibility between the kinase domains and 14-3-3 molecules (43). This step improved the density of the distal tail segment (Fig. S2D and E). All 3D classification and refinement steps were performed without applying symmetry constraints. A selection of particles corresponding to the best 3D class (113,313 particles) was used for 3D refinement, followed by CTF refinement and Bayesian polishing in Relion 3. The overall resolution was estimated based on the gold-standard Fourier shell correlation

(FSC) 0.143 criterion (Fig. S2F). A summary of the steps in the EM image processing procedures is shown in Fig. S2.

Model building and refinement

The N-terminal ~450 residues of Raf, which include the Ras-binding domain, were not visible in the cryo-EM map, and appear to be disordered. The N-terminal segment has an autoinhibitory function (44), and the fact that it cannot be visualized suggests that the structure represents an active assembly of B-Raf (45), consistent with the observed enzymatic activity of the sample (Fig. S1).

The B-Raf inhibitor Dabrafenib (46) was added to the insect cells during protein expression, but was not included in any of the buffers used for protein purification. The purified C-terminal fragment of B-Raf, at a concentration of 80 μ M, was analyzed by LC/MS and compared to LC/MS results for a control sample of Dabrafenib dissolved in S6 buffer at a concentration of 40 μ M, with no protein. The signal intensity for a peak corresponding to Dabrafenib in the B-Raf sample was only 0.3% of that for Dabrafenib in the control sample. Based on these results, we conclude that there is little or no Dabrafenib bound to the purified B-Raf. B-Raf kinase dimers in a structure of the B-Raf:MEK complex (PDB ID: 4MNE) (22) have no inhibitors bound, and so we used this structure as the starting model for interpreting the cryo-EM density. The kinase domains in the structure of the B-Raf:MEK complex are in the ON-state, and these coordinates fit readily into the cryo-EM map (Fig. S4A). We therefore conclude that both kinases in the cryo-EM model are in the ON-state conformation.

We fitted the coordinates of human 14-3-3 σ from a crystal structure of the complex with the Raf kinase C-terminal peptide (PDB ID: 4IEA) (47) into the cryo-EM map, and both 14-3-3 and the peptide molecules fit well into the electron density for each molecule in the dimer (Fig. S4B). For each kinase domain, there is well defined electron density for the C-terminal tail from the point where it emanates from the kinase domain and through the peptide-docking site in each 14-3-3 molecule (up to Leu⁷³³; denoted the proximal tail segment and the 14-3-3 binding element in Fig. 1A). The angles between the two 14-3-3 subunits vary in different crystal forms of 14-3-3 dimer crystal structures deposited in PDB, and the cryo-EM density matches one of the 14-3-3 dimer structures with the widest angle (PDB ID: 5D2D; human 14-3-3 ζ dimer in complex with CFTR (cystic fibrosis transmembrane conductance regulator) R-domain peptide (48)) (Fig. S4C).

Sequences of the 14-3-3 genes from *Spodoptera frugiperda* are not available. We compared the sequences of 14-3-3 ϵ and 14-3-3 ζ from *Spodoptera litura*, a close relative of *S. frugiperda*, and found that the residues that interact with Raf are identical in the two isoforms (Fig. S17), with ~70% sequence identity throughout the proteins. This indicates that the two 14-3-3 isoforms are interchangeable in terms of their interaction with B-Raf, and that the observed density most likely represents a superposition of the two isoforms. Therefore, we used the sequence of *S. litura* 14-3-3 ζ chain for both 14-3-3 molecules in the structure. The two 14-3-3 genes from *S. litura* share more than 80% sequence identity with the corresponding human genes, indicating that the complex of B-Raf with human 14-3-3 proteins will have essentially the same structure as that derived from our reconstruction.

Manual adjustment of the model was performed in Coot (49), followed by iterative rounds of real-space refinement in Phenix (50) and manual fitting in Coot. Model validation was done using statistics from Ramachandran plots and MolProbity scores in Phenix (Table S2). Structural models are visualized using ChimeraX (51) and PyMOL (The PyMOL Molecular Graphics System, Version 2.0 Schrödinger, LLC).

Kinase assays using purified B-Raf constructs

The purified full-length B-Raf protein, generated using intein chemistry as described above, was mixed in kinase assay buffer (20 mM Tris pH 8.0, 100 mM NaCl, 2 mM MgCl₂, 1 mM TCEP) with purified MEK1 (D190N mutant) protein with final concentrations of 100 nM (B-Raf) and 1 μM (MEK1). For assays using FLAG-tagged B-Raf constructs purified from HEK293T cells, as described above, the proteins were mixed with MEK1 in kinase assay buffer with final concentrations of 10 nM (B-Raf) and 1 μM (MEK1). The samples were incubated at 30°C, and the phosphorylation reactions were initiated by the addition of ATP to a final concentration of 1 mM. Aliquots were taken from the reaction solution at various time points and mixed with quenching solution, SDS-PAGE loading buffer supplemented with 20 mM EDTA, to achieve final concentration of 1% SDS and 10 mM EDTA in the quenched solutions. The samples were analyzed by SDS-PAGE gel electrophoresis followed by Western blot analysis using phospho-MEK antibody (Cell Signaling Technology, #9121).

Cellular signaling assay

The human B-Raf gene was cloned into the pEGFP-N1 plasmid (Clontech) to make B-Raf mutants fused to an N-terminal eGFP tag. The mutations were introduced by QuikChange site-directed mutagenesis (Stratagene). In addition to the mutations described in the main text, two hydrophobic residues from the distal tail segment that are located within the active site of B-Raf^{IN} in the structural model were replaced simultaneously by glycine (L745G and Y746G (LYGG)), or six residues in the distal tail segment were replaced by glycine or serine (E741G/D742G/F743S/L745G/Y746G, (GGSSGG)).

Ba/F3 cells were cultured in RPMI medium containing 10% FBS, 1% penicillin/streptomycin, and 10 ng/ml murine interleukin 3 (mIL-3) (PeproTech Catalog# 213-13; 1:1000 dilution of stock 100 μg/ml). Cells were transfected in Transfection Media (RPMI with 10% FBS, no penicillin/streptomycin) using BioRad Gene Pulser Xcell (settings: 250 V, 975 μF, infinity resistance, 4 mm cuvette). 20 μg DNA was used for 20 million cells. Cells were then incubated for 18-20 hours in Transfection Media containing 10 ng/ml mIL-3. Cells were harvested and washed with 1% PBS twice, and then resuspended in plain RPMI medium for rest before stimulation. Cells were rested at a concentration of 1 million cells/100 μl RPMI medium per well for 4 hours in a 96-well (round-bottom) plate. Cells were stimulated by adding 50 μl of mIL-3 (90 ng/ml). Stimulations were stopped by fixing with 50 μl of 8% paraformaldehyde (PFA) and incubating for 20 minutes. PFA was removed and cells were permeabilized by adding 200 μl of 90% methanol and stored at -20 °C overnight. Intracellular staining was done using pERK (1/2)

primary antibody (Cell Signaling Technology; Product #9106; 1:200 dilution) and PE-Conjugated Goat Anti-Mouse secondary antibody (Jackson Laboratories; Code 115-116-146; 1:200).

Flow data was analyzed using FlowJo software (FlowJo, LLC). Histograms were plotted and the statistical significance was calculated using multiple t test (without any corrections and alpha at 0.05) in the GraphPad Prism software (GraphPad Software).

Molecular Dynamics simulations

Preparation of Structural Models for Simulations

We built two systems corresponding to the cryo-EM model, one with the distal tail segment of B-Raf^{OUT} present, and one in which this segment was deleted. The cryo-EM model has been refined at relatively low resolution, and small inaccuracies in the model can generate large forces in simulations. To avoid possible instabilities in the trajectories, we replaced parts of the cryo-EM model with the corresponding high-resolution crystallographic coordinates, where possible. The kinase dimer was from the structure of B-Raf bound to MEK (PDB ID: 4MNE) (22) - chains B and C were used for the simulation model. Residues in the phosphate-binding loop in the N-lobe (residues 464 to 468) are missing in this crystal structure and were modelled based on the structure of protein kinase A (PDB ID: 1ATP) (52). Residues 603 to 609 in the activation loop are missing in chain C of the B-Raf structure (PDB ID: 4MNE) and were modelled based on the structure of the activation loop in chain B. The coordinates for the 14-3-3 binding element (residues 726 to 731) was taken from the structure of a Raf-peptide complex with 14-3-3 σ (PDB ID: 4IEA) (47). This segment includes a phosphorylated serine at position 729 (charge -2). The proximal tail segment, remaining portions of the 14-3-3 binding element, and the distal tail segment of B-Raf^{OUT} were taken from the cryo-EM model. The side-chain rotamers were chosen arbitrarily for residues where there is no clear cryo-EM density for the sidechains. The ends of the kinase domains were capped with acetyl and N-methylamide groups at the N-terminal and C-terminal residues, respectively.

The 14-3-3 dimer was taken from the crystal structure of the human 14-3-3 ζ homodimer (PDB ID: 5D2D) (48). Residue 70 in one chain and residues 70 to 72 in the second chain are missing in the crystal structure, and were built with Coot (49). The C-terminal tail of 14-3-3 (residues 230 to 245) is not present in the crystal structure, and no interpretable density is present for this segment in the cryo-EM density. This segment was modelled in an arbitrary conformation for each 14-3-3 protomer, using Coot. The terminal residues of the 14-3-3 dimer chains were uncapped since these are the actual termini of the polypeptide chain. Water molecules present in the crystal structures were retained.

Simulation Protocol

Both systems were solvated with TIP3 water (53) and ions were added so that the final ionic strength was 150 mM, using with VMD (54). The energy of each system was minimized first for 1000 steps holding the protein chains fixed, then allowing all the atoms to move. For molecular dynamics trajectories, each system was equilibrated for 1 ns holding the protein heavy atoms fixed, then for 1 ns holding the backbone atoms fixed and then for 1 ns while allowing all the atoms to

move, followed by production runs. Three production trajectories, each 500 ns long, were generated for each system. All equilibration runs and production runs were performed at constant temperature (300 K) and pressure (1 atm).

5 The simulations were carried out with the NAMD package (55) using the CHARMM36m force-field (56) using an integration timestep of 2 fs. The Particle Mesh Ewald approximation was used to calculate long-range electrostatic energies (57) with a grid size of 1 Å. All hydrogens bonded to heavy atoms were constrained with the ShakeH module. Van der Waal's interactions were truncated at 12 Å. The Langevin thermostat was used to control the temperature with a damping coefficient of 1/ps, applied only to non-hydrogen atoms. Pressure was controlled by the Nose-Hoover Langevin method (58, 59) with a Langevin piston period of 200 fs and a piston decay time of 50 fs. For the analyses, the trajectories were sampled every 8 ps. Distances were calculated using the CPPTRAJ module of AmberTools18 (60).

10

Figure S1.

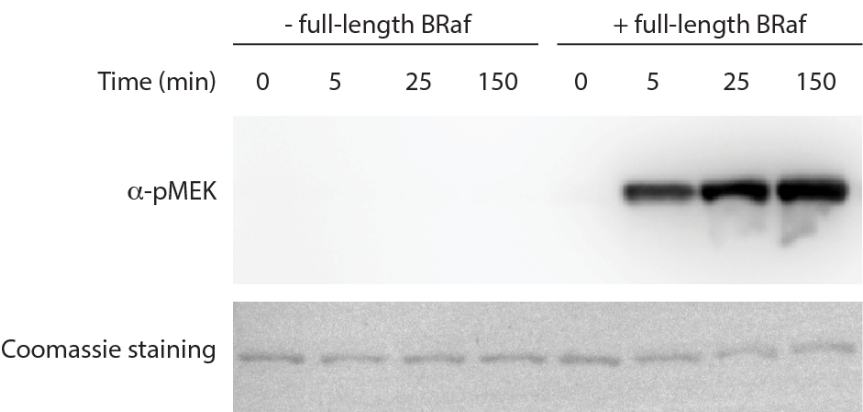
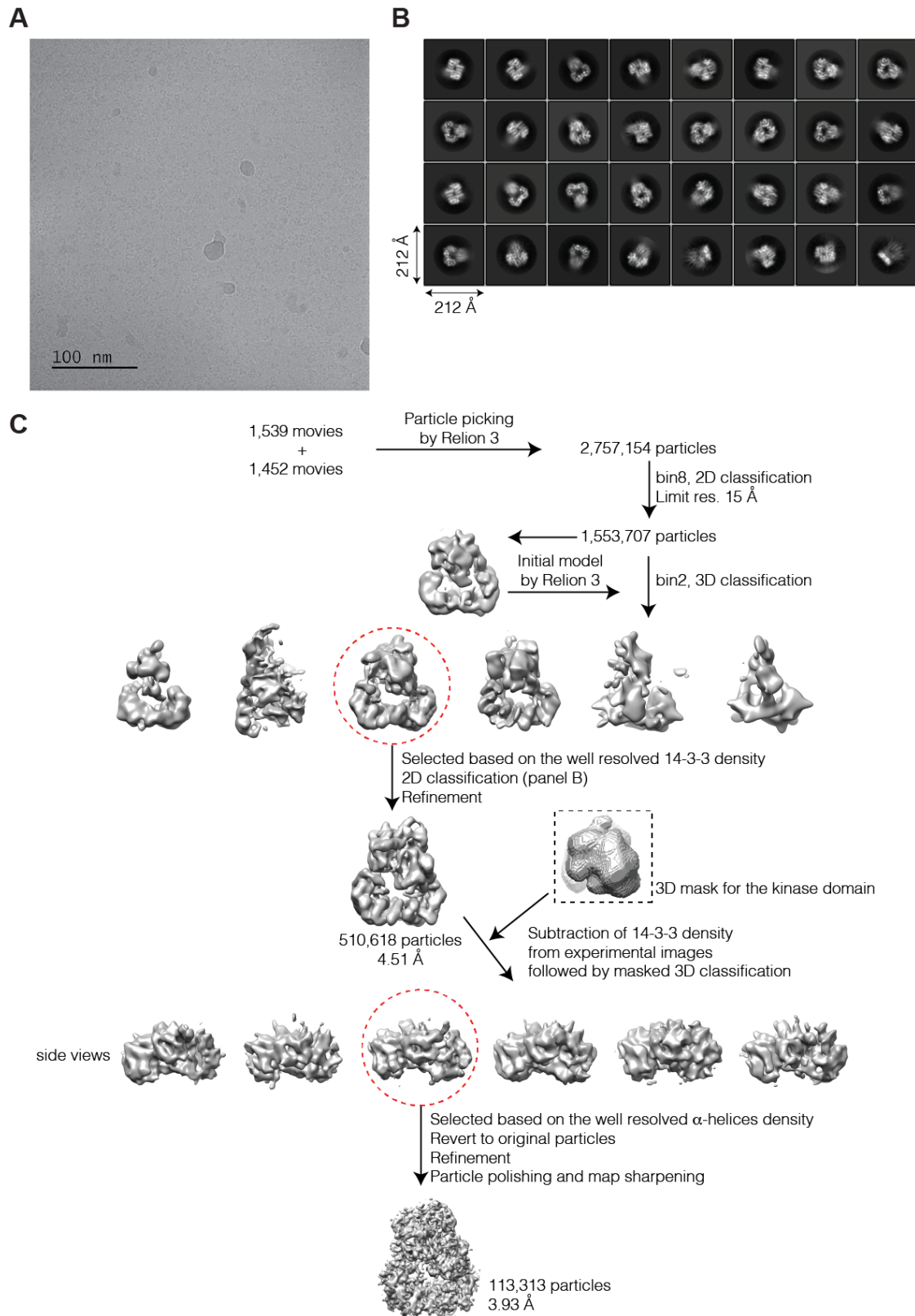


Fig. S1. MEK1 phosphorylation by purified full-length B-Raf. SDS-PAGE gel analysis of MEK1 phosphorylation with or without addition of purified full-length B-Raf. Kinase-dead MEK1 D190N mutant (residues 37-393) was analyzed with or without B-Raf. The reaction was initiated by the addition of ATP to the solution. Aliquots were taken out for SDS-PAGE analysis at indicated time points, and the kinase reaction was quenched by the addition of SDS-loading buffer supplemented with EDTA. The result was analyzed by western blotting using phospho-MEK antibody first (top panel) and the same membrane was stained by Coomassie Brilliant Blue (bottom).

Figure S2.



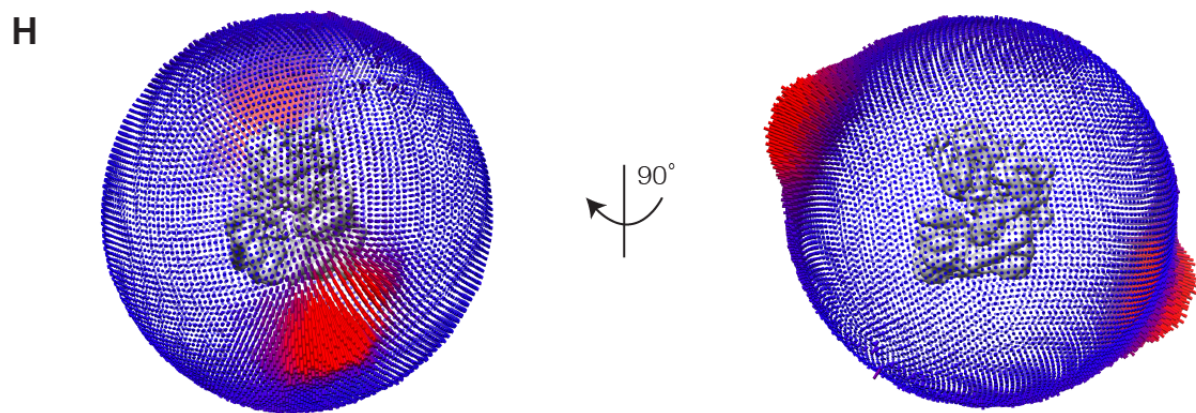
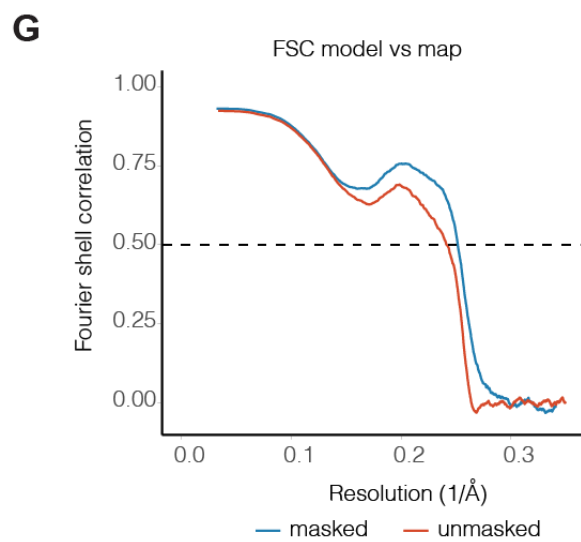
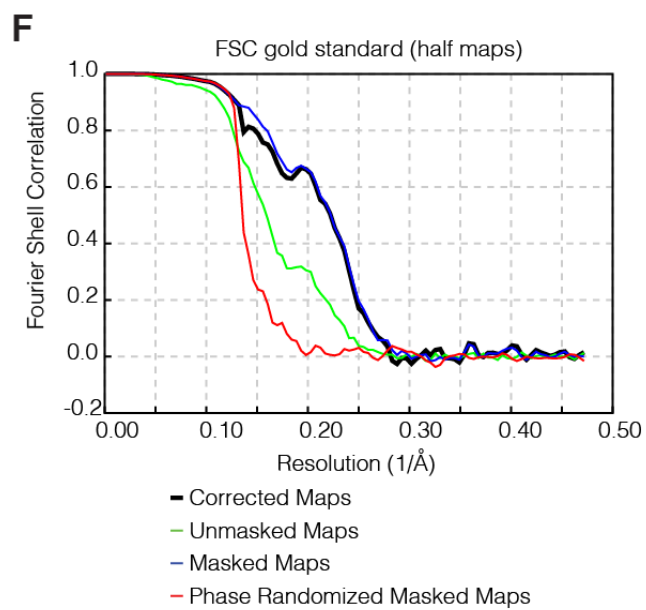
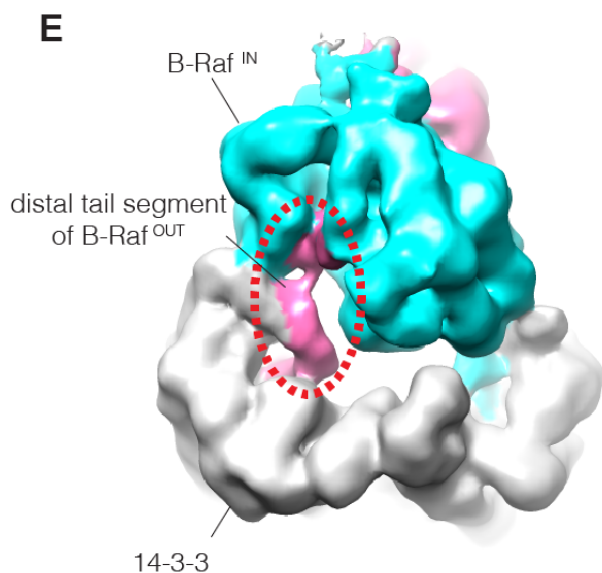
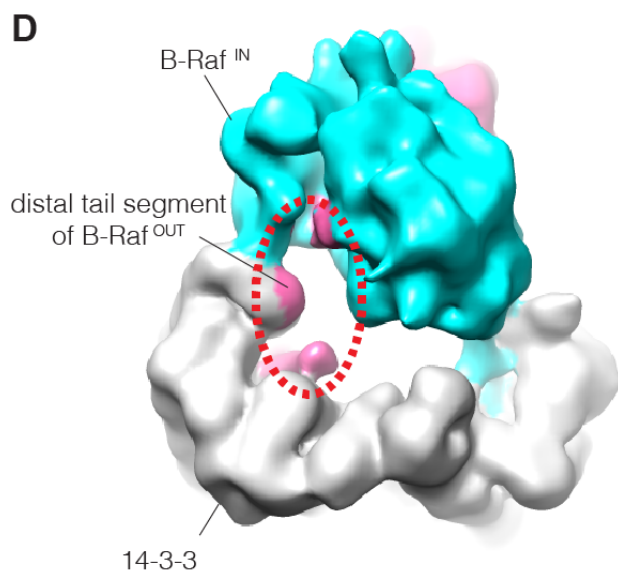
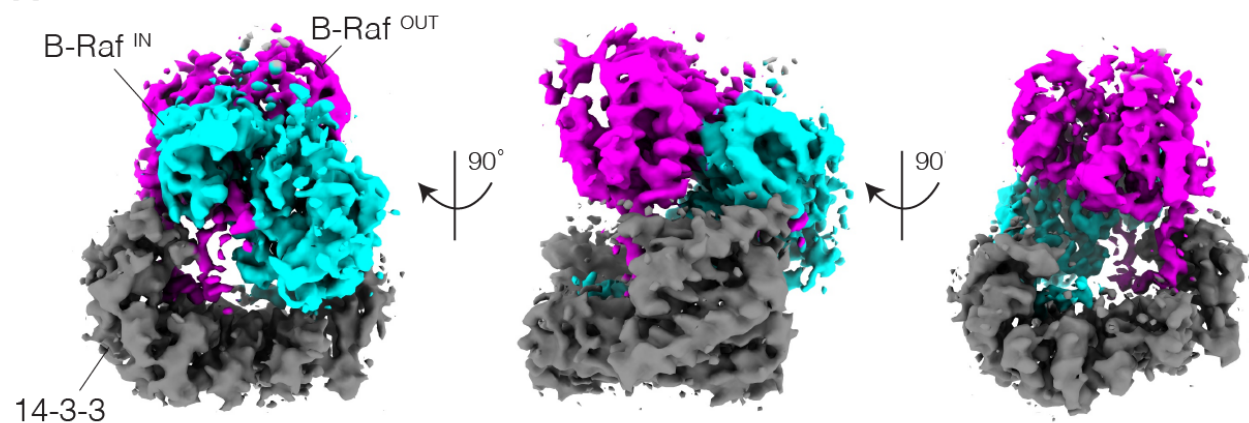


Fig. S2. Cryo-EM image processing. (A) Representative electron micrograph. (B) Representative 2D class averages obtained from reference-free 2D classification. (C) Summary of classification and refinement procedures. (D and E) Comparison of the cryo-EM maps for the B-Raf:14-3-3 complex, with or without 3D classification following signal subtraction of the 14-3-3 density. The results of 3D auto-refinement before (panel A) and after (panel B) 3D classification with 3D mask at the kinase domain are shown. The 14-3-3 density was subtracted from the particle images by Relion 3.0 before the 3D classification. The unsharpened map is shown here, and the cryo-EM map was colored the same way as Fig. 1B. The density corresponding to the distal tail segment of B-Raf^{OUT} is highlighted by a circle. (F) Fourier shell correlation (FSC) curves obtained from Relion 3 postprocess job. The resolution is estimated at FSC = 0.143. (G) Fourier shell correlation (FSC) curves obtained from Phenix refinement job. (H) The angular distribution of the final reconstruction obtained from Relion.

Figure S3.

A



B

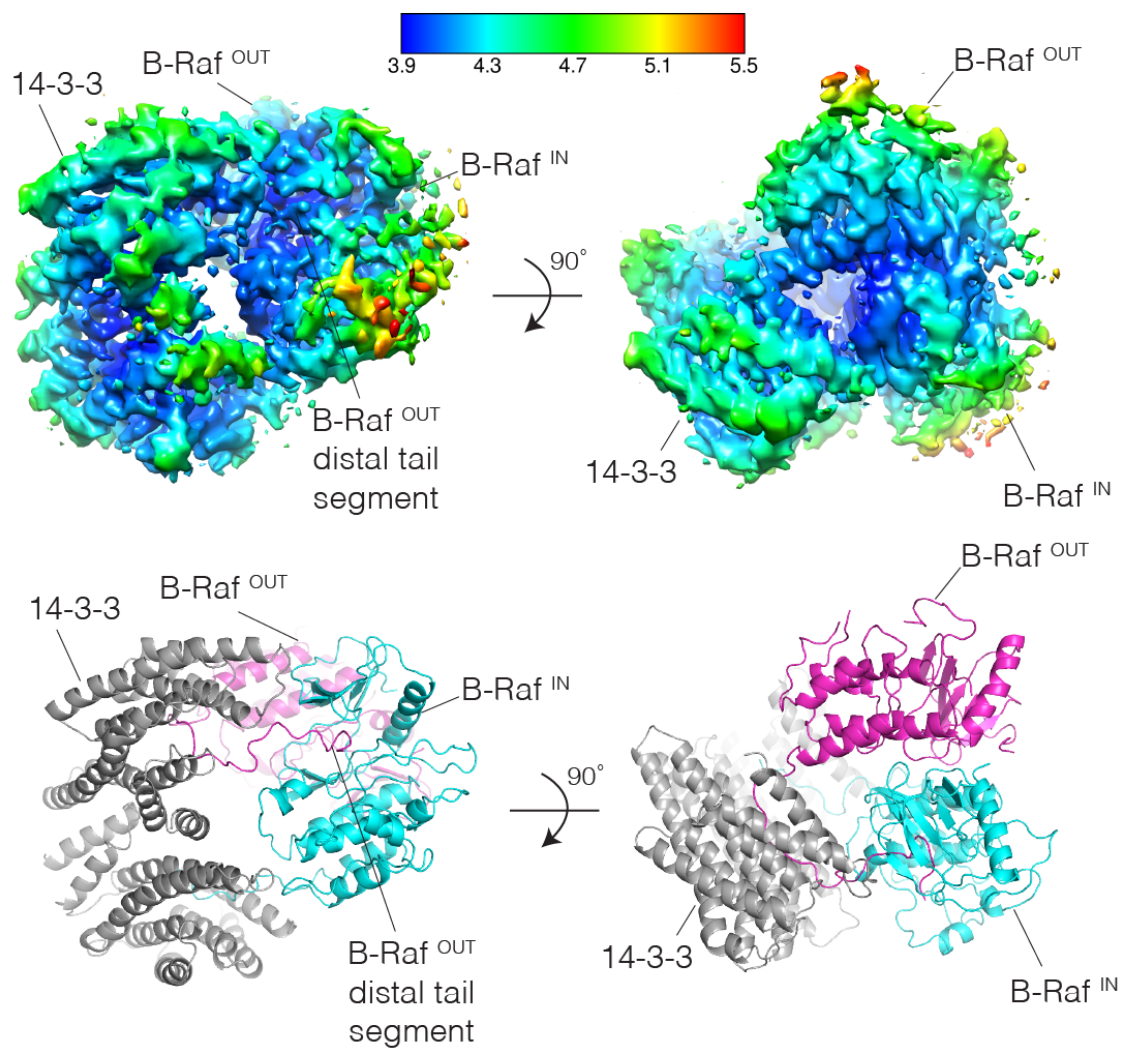
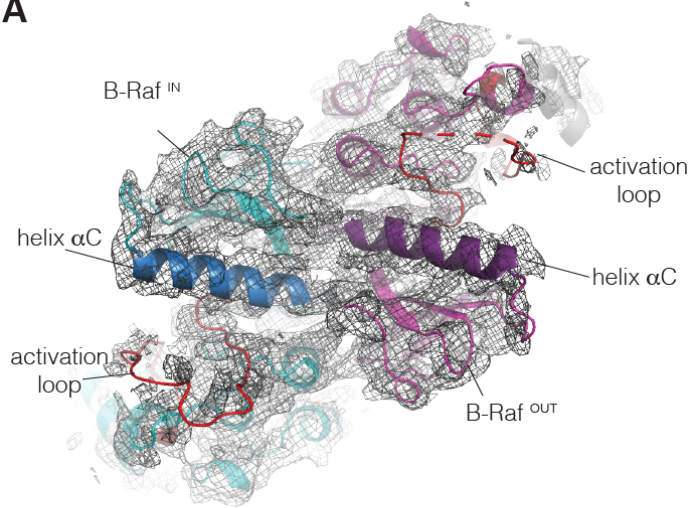


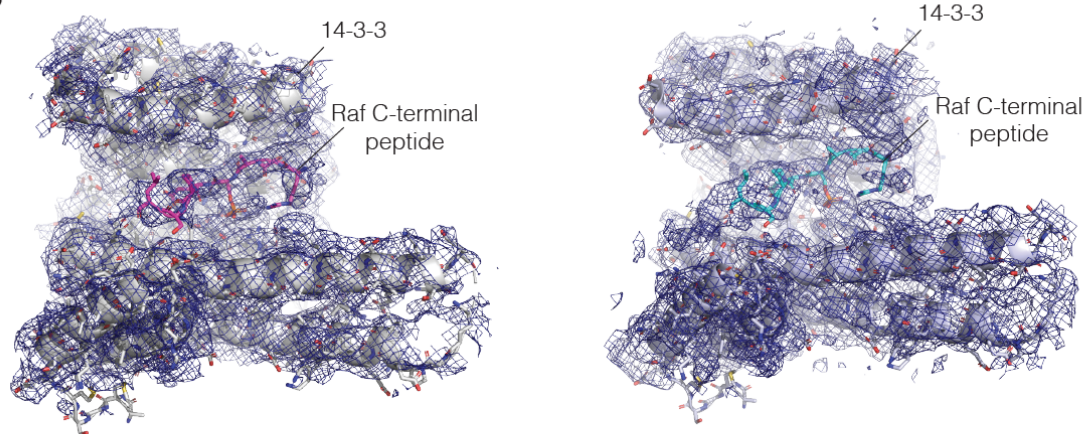
Fig. S3. Cryo-EM reconstruction of the B-Raf:14-3-3 complex. (A) The cryo-EM map of the B-Raf:14-3-3 complex colored the same way as Fig. 1B. (B) The cryo-EM map of the B-Raf:14-3-3 complex colored by the local resolution estimated by Relion 3 (40) is shown in two orthogonal views at the top. The color scale corresponding to the local resolution is shown above the electron density maps. The cryo-EM model of the B-Raf:14-3-3 complex is shown below the corresponding views of the cryo-EM map.

Figure S4.

A



B



C

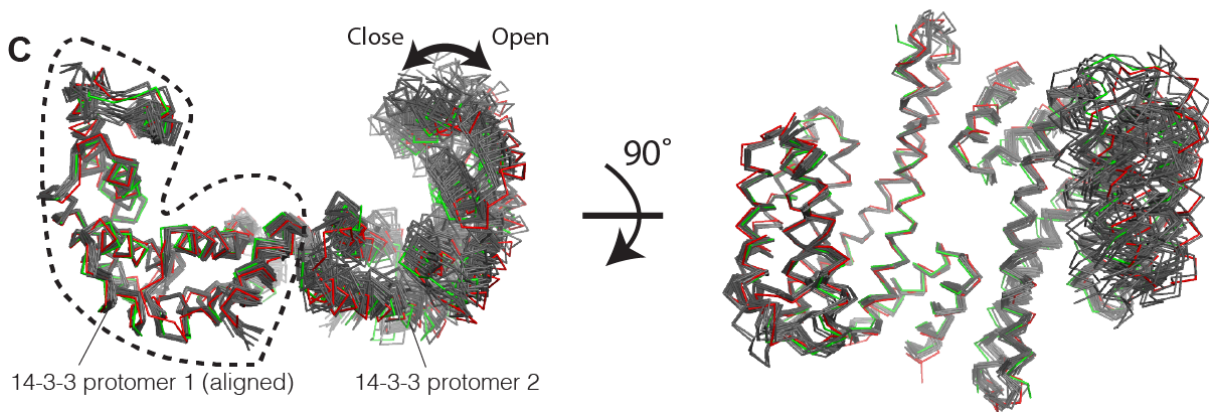


Fig. S4. Correspondence between the cryo-EM map and the crystal structures used to build the cryo-EM model. (A) Coordinates for the B-Raf kinase dimer are taken from the crystal structure of the B-Raf:MEK complex (PDB ID: 4MNE) (22) and fit into the cryo-EM map using chimera (61). Helix G of B-Raf^{OUT} has weak density and is shown in gray. (B) A crystal structure

of a 14-3-3 σ and Raf C-terminal peptide complex (PDB ID: 4IEA) (47) is fit into the cryo-EM map corresponding to each 14-3-3 molecule in the cryo-EM map, respectively. (C) The comparison of the angles between two subunits in the 14-3-3 dimers. Structural models of fifteen human 14-3-3 ζ homodimers (gray) from 12 different crystal structures with unique space group (PDB IDs: 1IB1, 1QJA, 2C1N, 3RDH, 4HKC, 4N7G, 4ZDR, 5D2D, 5D3F, 4N7Y, 6EJL, 6F09) as well as 14-3-3 σ homodimer with the Raf C-terminal phosphopeptide (PDB ID: 4IEA, green) and the cryo-EM structure (red) were aligned using only one protomer (dashed line). The positions of the other protomer varies relative to the aligned protomers and the variation is highlighted by the arrow.

10

Figure S5.

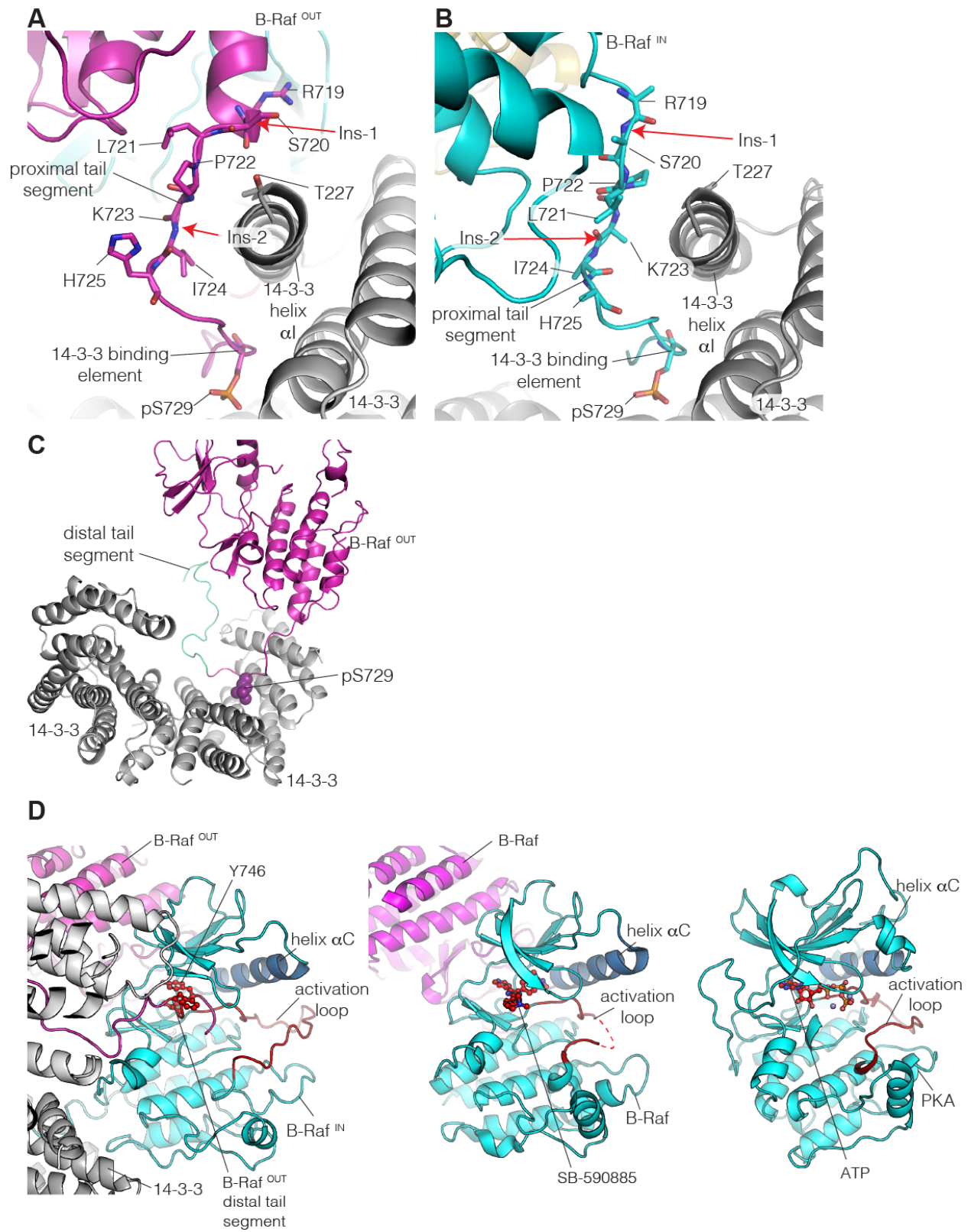


Fig. S5. Interactions formed by the B-Raf C-terminal tail. Interactions of the proximal tail segments of B-Raf^{OUT} (A) and B-Raf^{IN} (B) with 14-3-3. The 14-3-3 binding elements of each B-Raf molecule are also shown. Ins-1 and Ins-2 indicate (GSGSGS) residues insertion sites to generate the mutants for the cell-based assay. (A) The sidechain of Thr²²⁷ of 14-3-3 and the carbonyl group of Arg⁷¹⁹, the last turn of helix α I in B-Raf^{OUT}, are located in close proximity. (C) Disposition of the B-Raf^{OUT} distal tail segment with respect to the docking of the B-Raf tail on 14-3-3. The distal tail segment is highlighted in green. (D) Comparison of the positions of the B-Raf^{OUT} distal tail segment in the B-Raf:14-3-3 complex, the small molecule inhibitor, SB-590885, in the B-Raf dimer (PDB ID: 2FB8) (21), and the ATP molecule in the prototypical PKA structure (PDB ID: 1ATP) (52).

Figure S6.

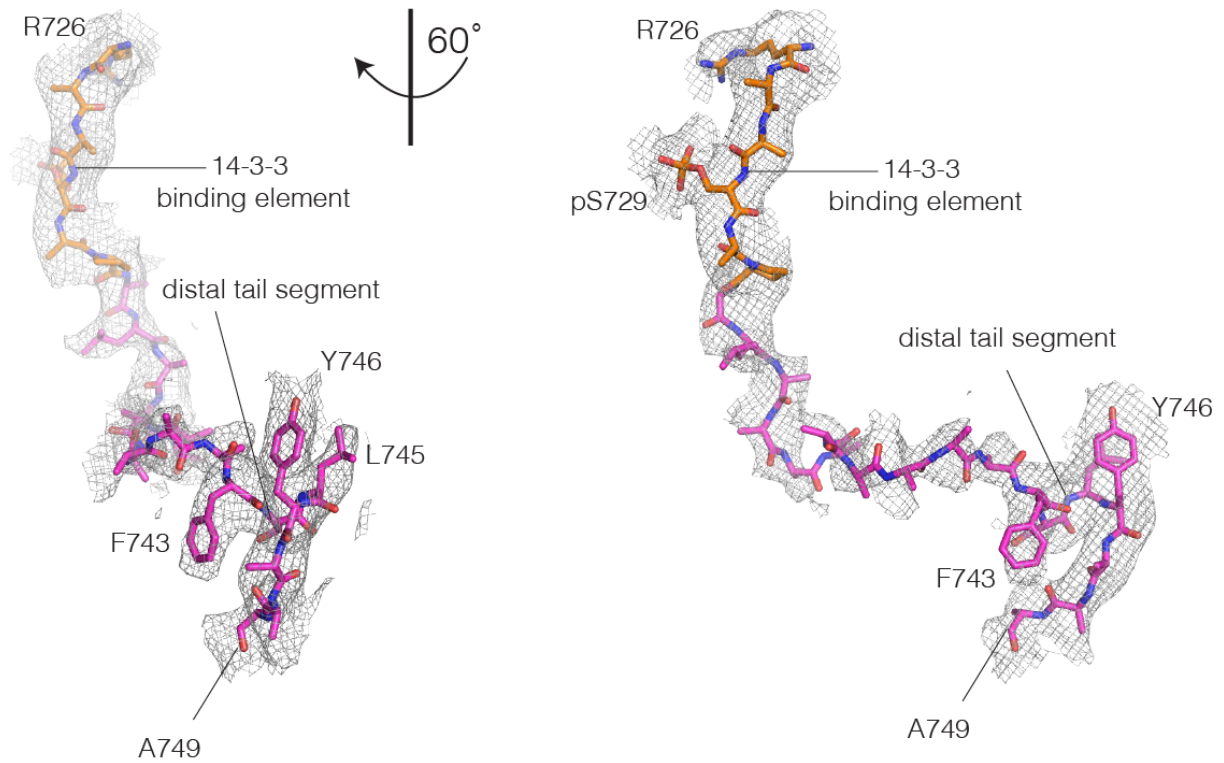


Fig. S6. Cryo-EM density for the 14-3-3 binding element and the distal tail segment of B-Raf^{OUT}. The structural model and the cryo-EM density corresponding to the C-terminal tail of B-Raf^{OUT}. Residues from Arg⁷²⁶ to Ala⁷⁴⁹ are shown, spanning the 14-3-3 binding element (orange) and the distal tail segment (magenta).

Figure S7.

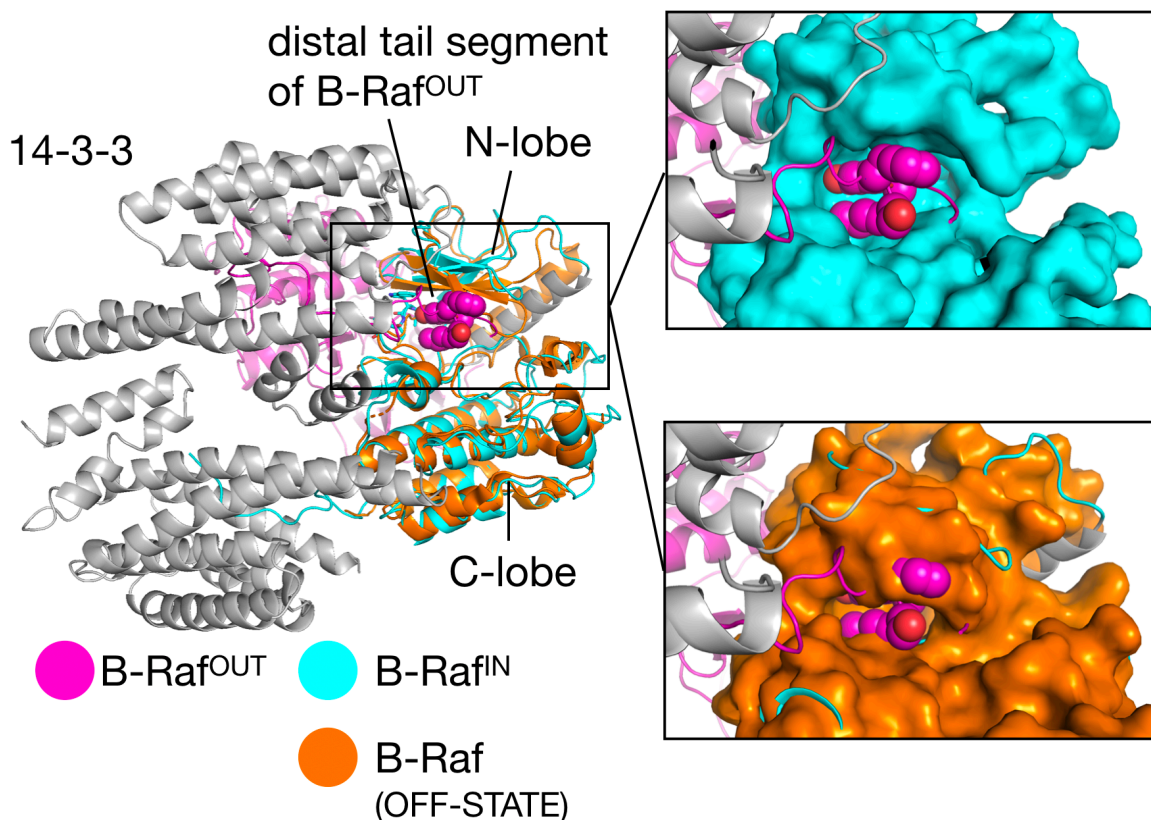


Fig. S7. Comparison of B-Raf^{fN} and B-Raf Cdk/Src OFF-state. The cryo-EM structure of the B-Raf:14-3-3 complex (cyan, magenta and gray) and the structure of B-Raf in the Cdk/Src OFF-state conformation (orange; PDB ID: 4WO5) (*16*) are superimposed on the kinase domains. A small molecule inhibitor that is bound to the kinase domain in the Cdk/Src OFF-state conformation has been removed for clarity. The surfaces of the kinase domains are shown in the two closeup views. In the cryo-EM structure, note that the distal tail segment of B-Raf^{fN} (cyan) packs closely within the active site of the kinase domain of B-Raf^{OUT} (magenta). In the Cdk/Src OFF-state, closure of the N-lobe of the kinase domain against the C-lobe would lead to severe steric clashes with the distal tail segment.

Figure S8.

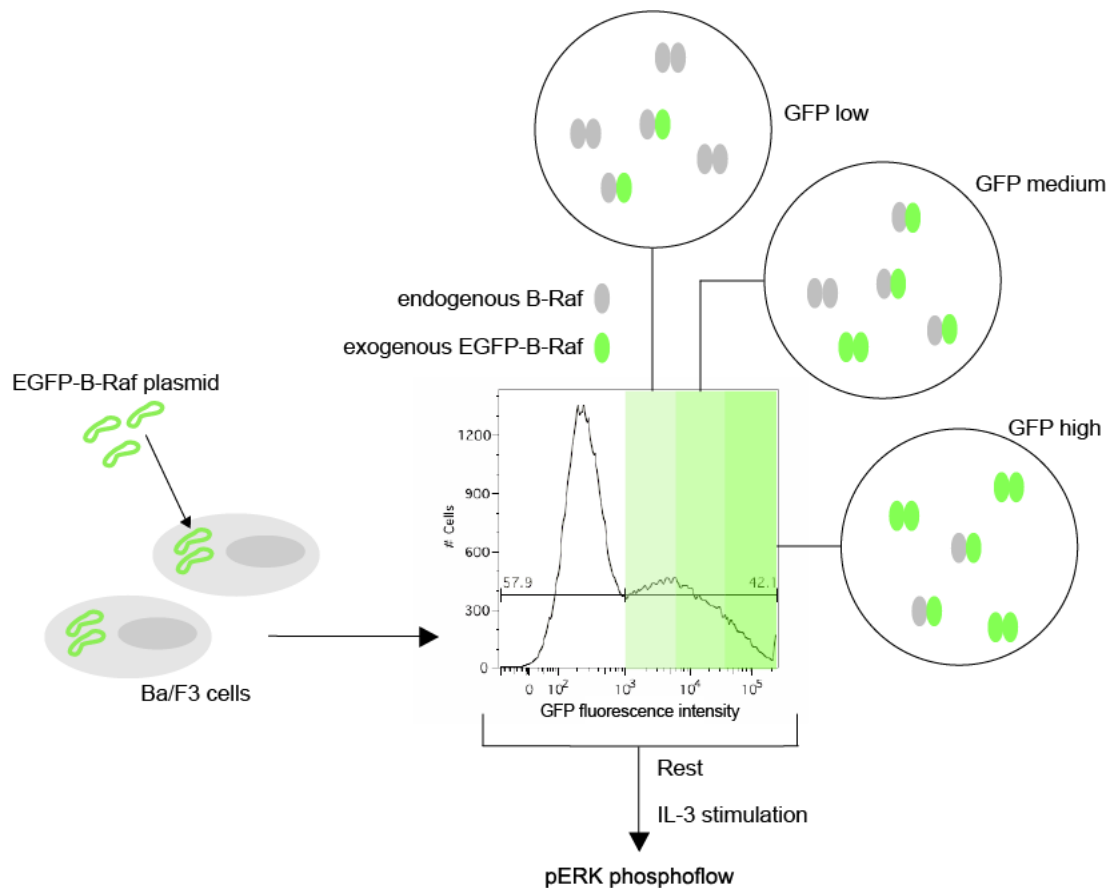
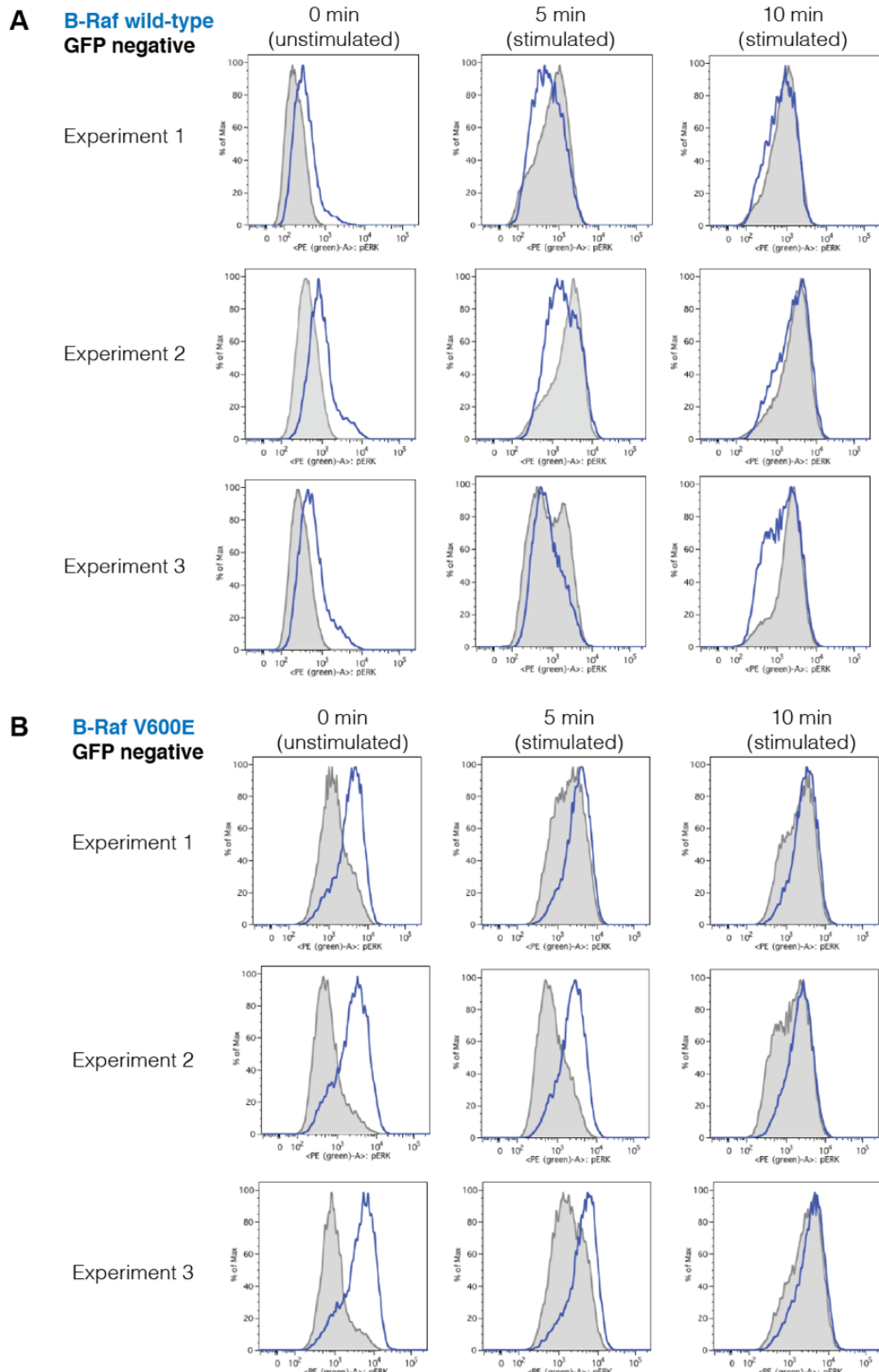
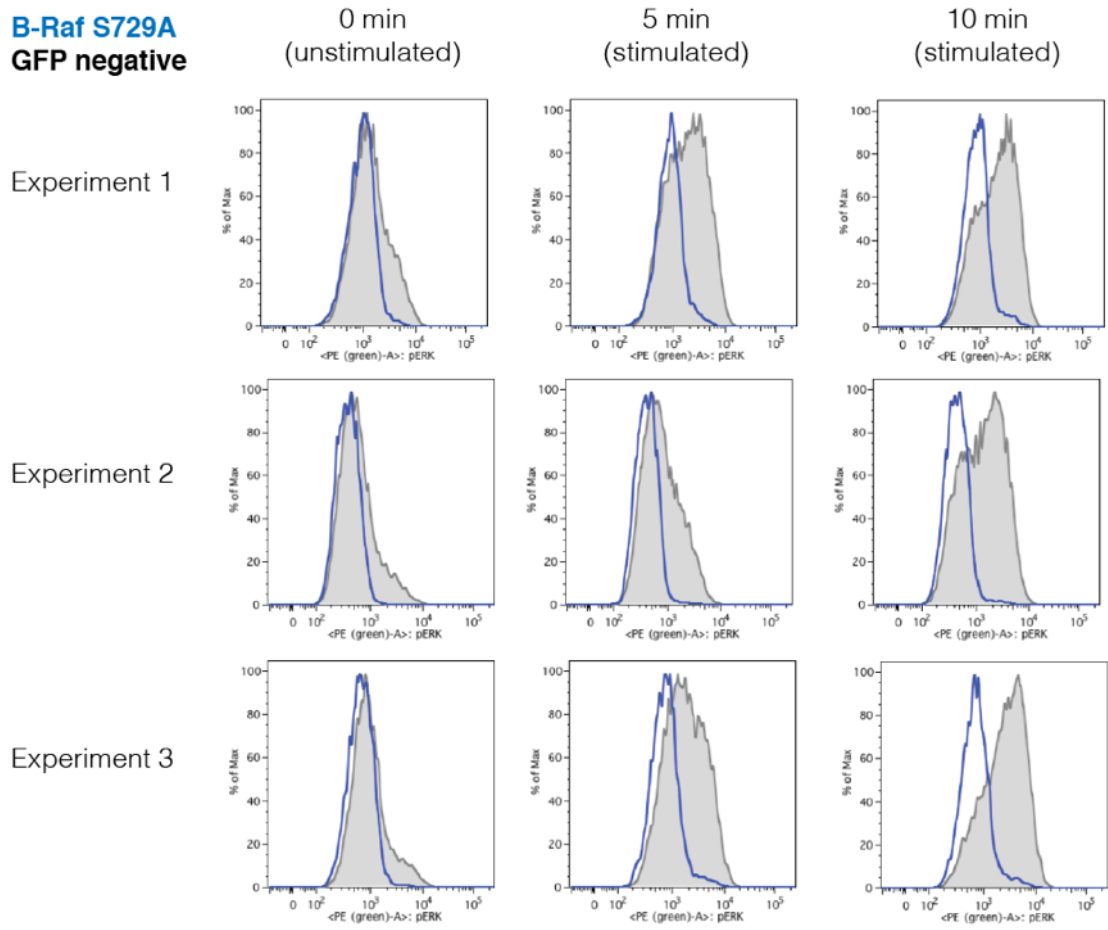


Fig. S8. Schematic diagram of the cell-based assay. Ba/F3 cells were transfected with peGFP-N1 vector, to make B-Raf protein fused to EGFP at the N-terminus. The cells were sorted by different EGFP expression levels using flow cytometry, and the distribution of the cells with various phospho-ERK levels is graphed.

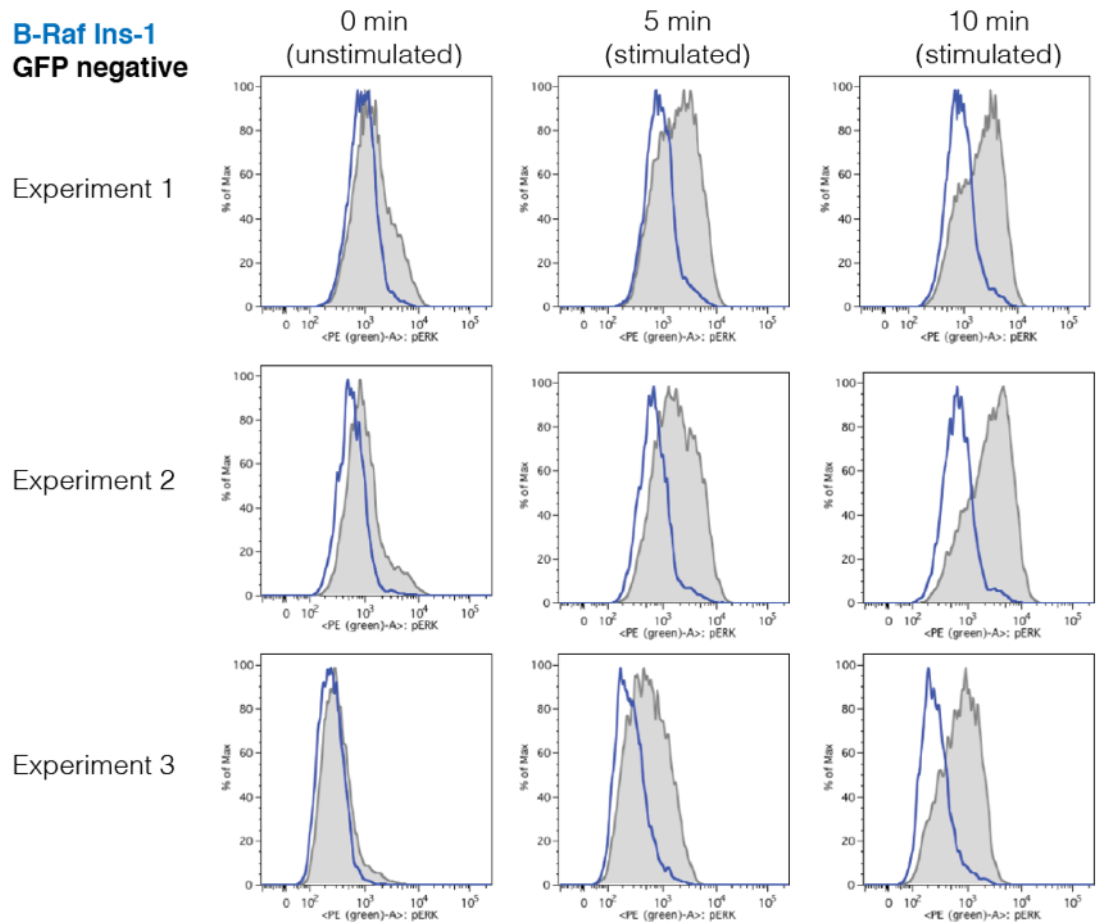
Figure S9.



C **B-Raf S729A**
GFP negative

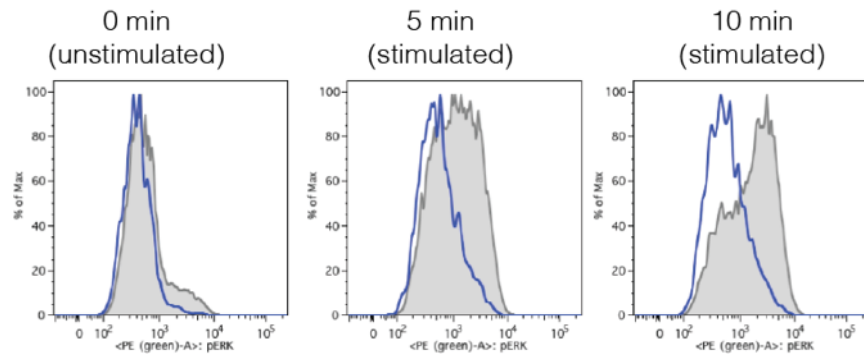


D **B-Raf Ins-1**
GFP negative

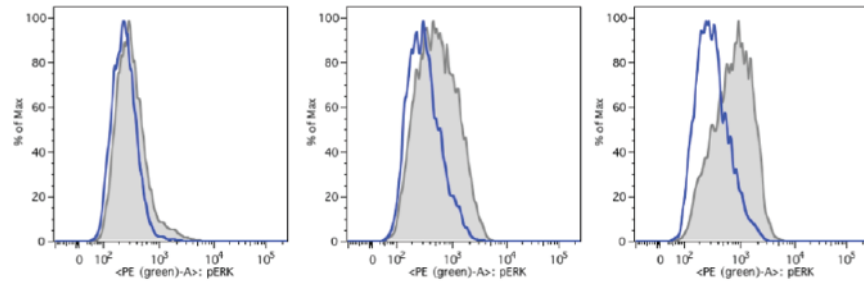


E **B-Raf Ins-2**
GFP negative

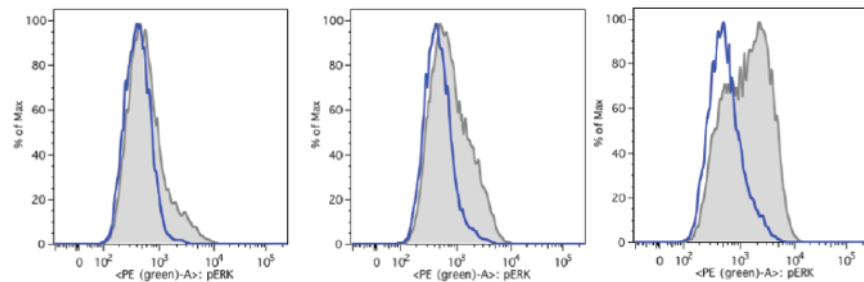
Experiment 1



Experiment 2

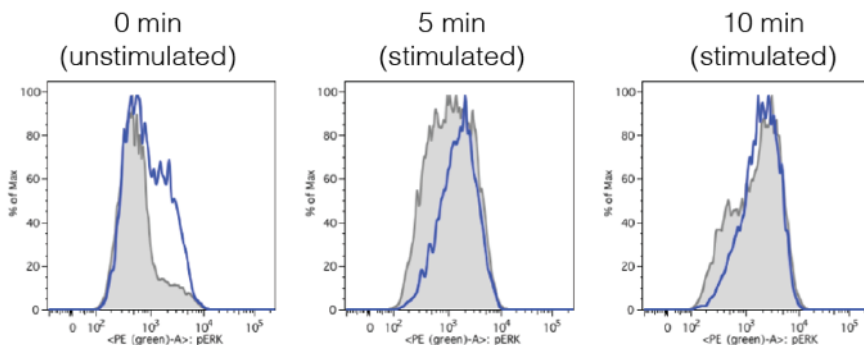


Experiment 3

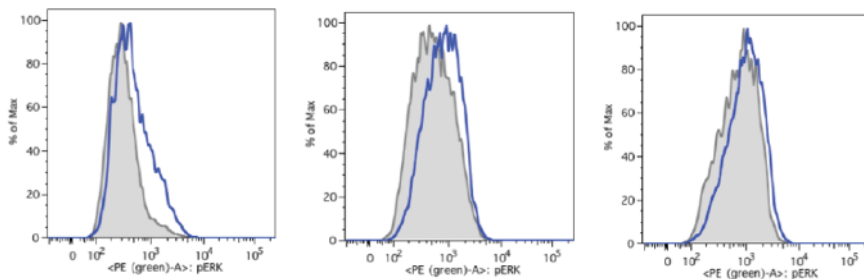


F **B-Raf Ins-3**
GFP negative

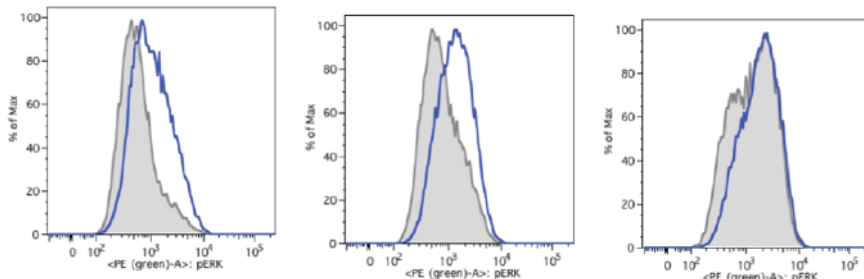
Experiment 1



Experiment 2

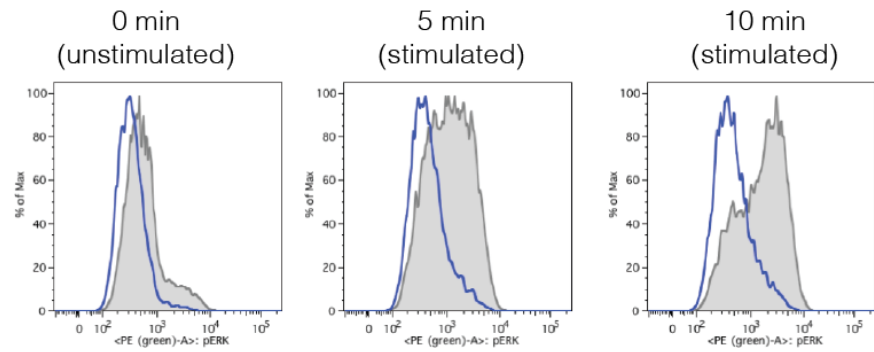


Experiment 3

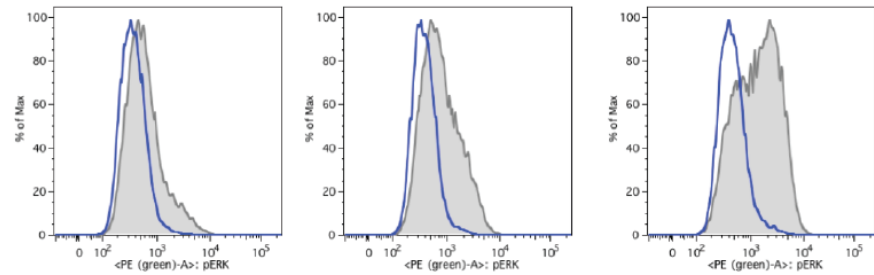


G **B-Raf L721G**
GFP negative

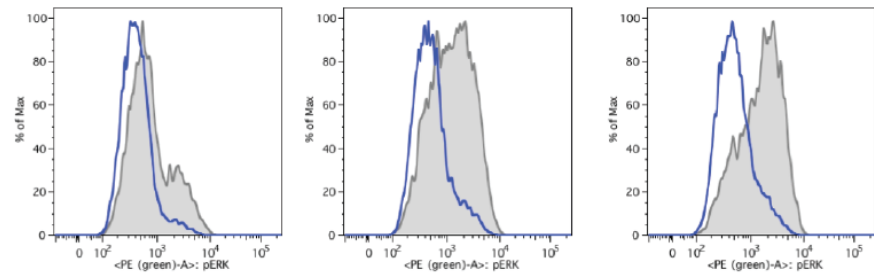
Experiment 1



Experiment 2

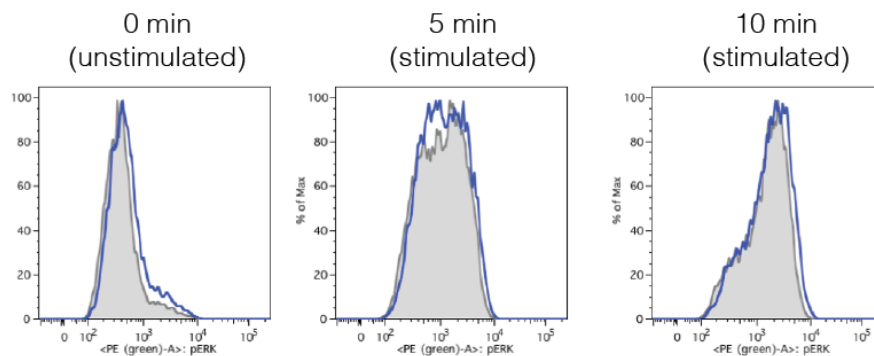


Experiment 3

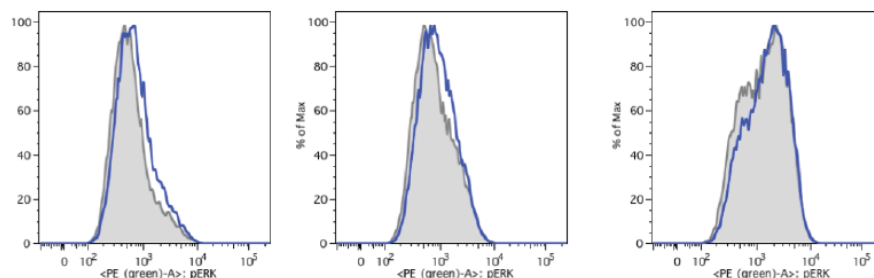


H **B-Raf ΔDTS**
GFP negative

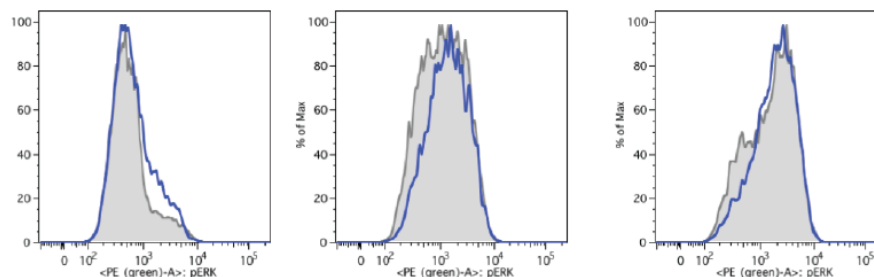
Experiment 1



Experiment 2

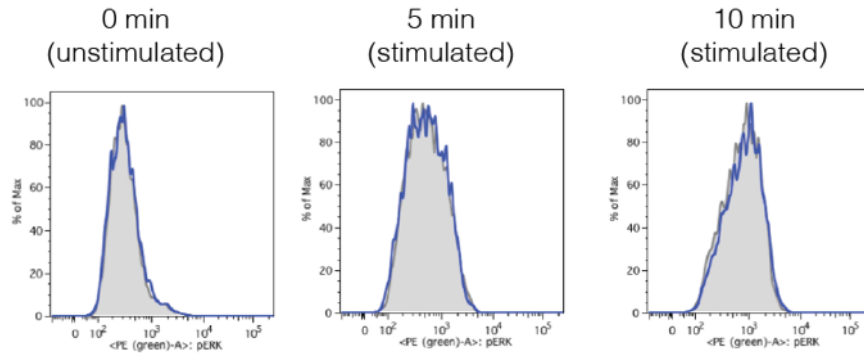


Experiment 3

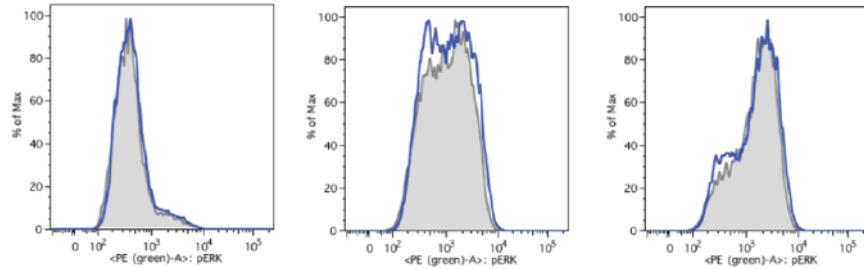


I **B-Raf LYGG**
GFP negative

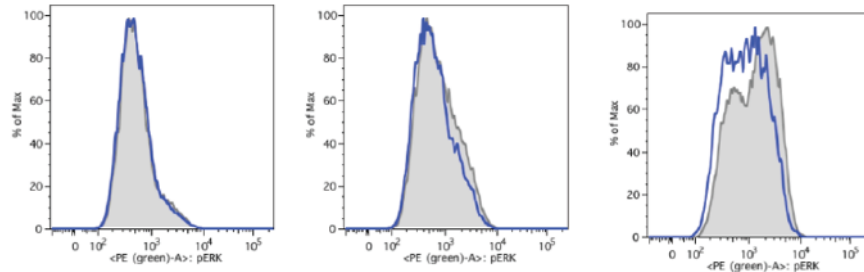
Experiment 1



Experiment 2

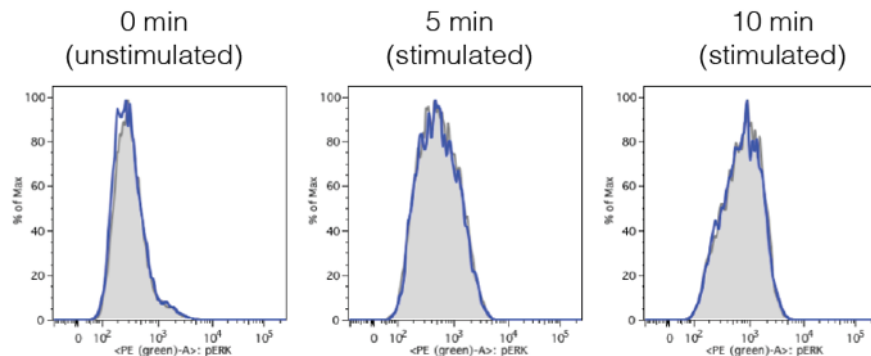


Experiment 3

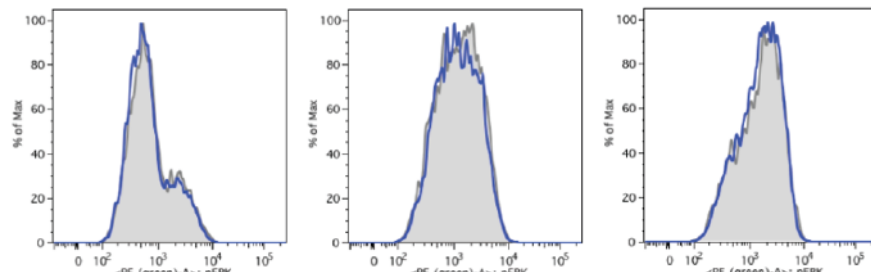


J **B-Raf GGSSGG**
GFP negative

Experiment 1



Experiment 2



Experiment 3

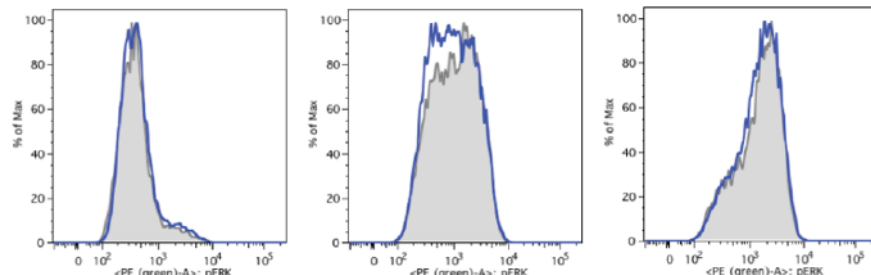


Fig. S9. Analysis of pERK levels upon expression of B-Raf. (A-J) Histograms of Ba/F3 cells with different phospho-ERK levels. The Ba/F3 cells were transfected with N-terminally EGFP-tagged wild-type B-Raf protein (A) or B-Raf variants (B-J) (blue lines) to compare to the endogenous signaling strength (GFP negative; gray lines). Each experiment was repeated more than three times and three representative results are shown here.

Figure S10.

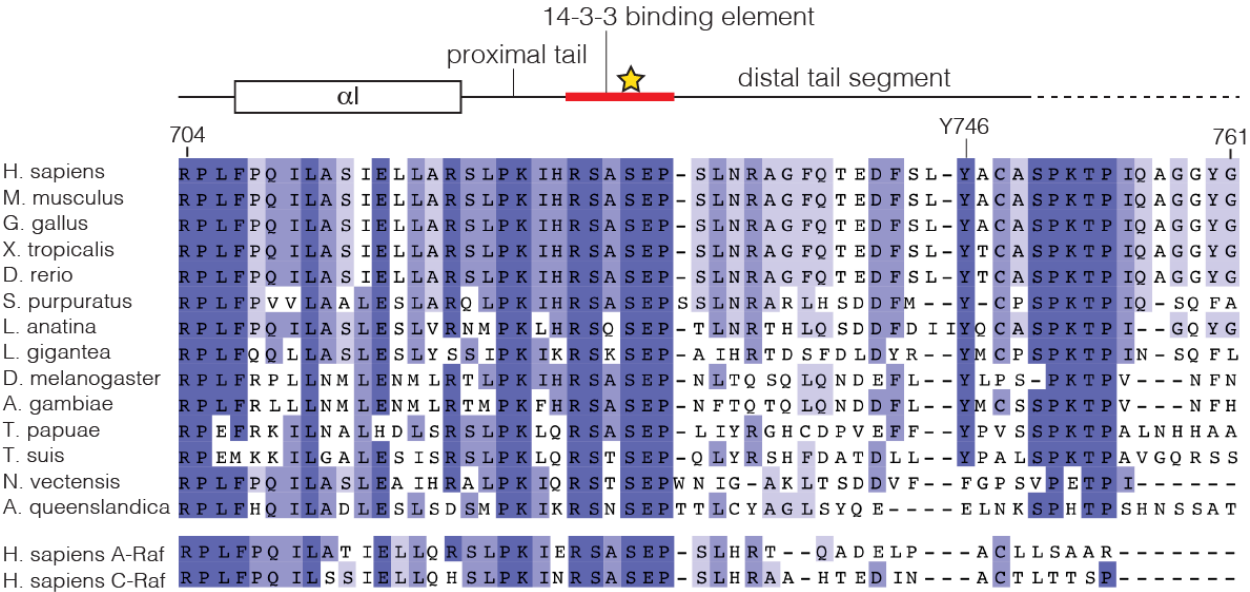


Fig. S10. Sequences of the C-terminal tail segments of Raf. Shown here is an alignment of the sequences of the C-terminal tail segments of B-Raf homologs from 14 metazoan species at the top, and human A-Raf and C- Raf at the bottom. αI is the last alpha-helix of the kinase domain. Species in the sequence alignments are *Homo sapiens*, *Mus musculus*, *Gallus gallus*, *Xenopus tropicalis*, *Danio rerio*, *Strongylocentrotus purpuratus*, *Lingula anatine*, *Lottia gigantea*, *Drosophila melanogaster*, *Anopheles gambiae*, *Trichinella papuae*, *Trichuris suis*, *Nematostella vectensis*, and *Amphimedon queenslandica*.

Figure S11.

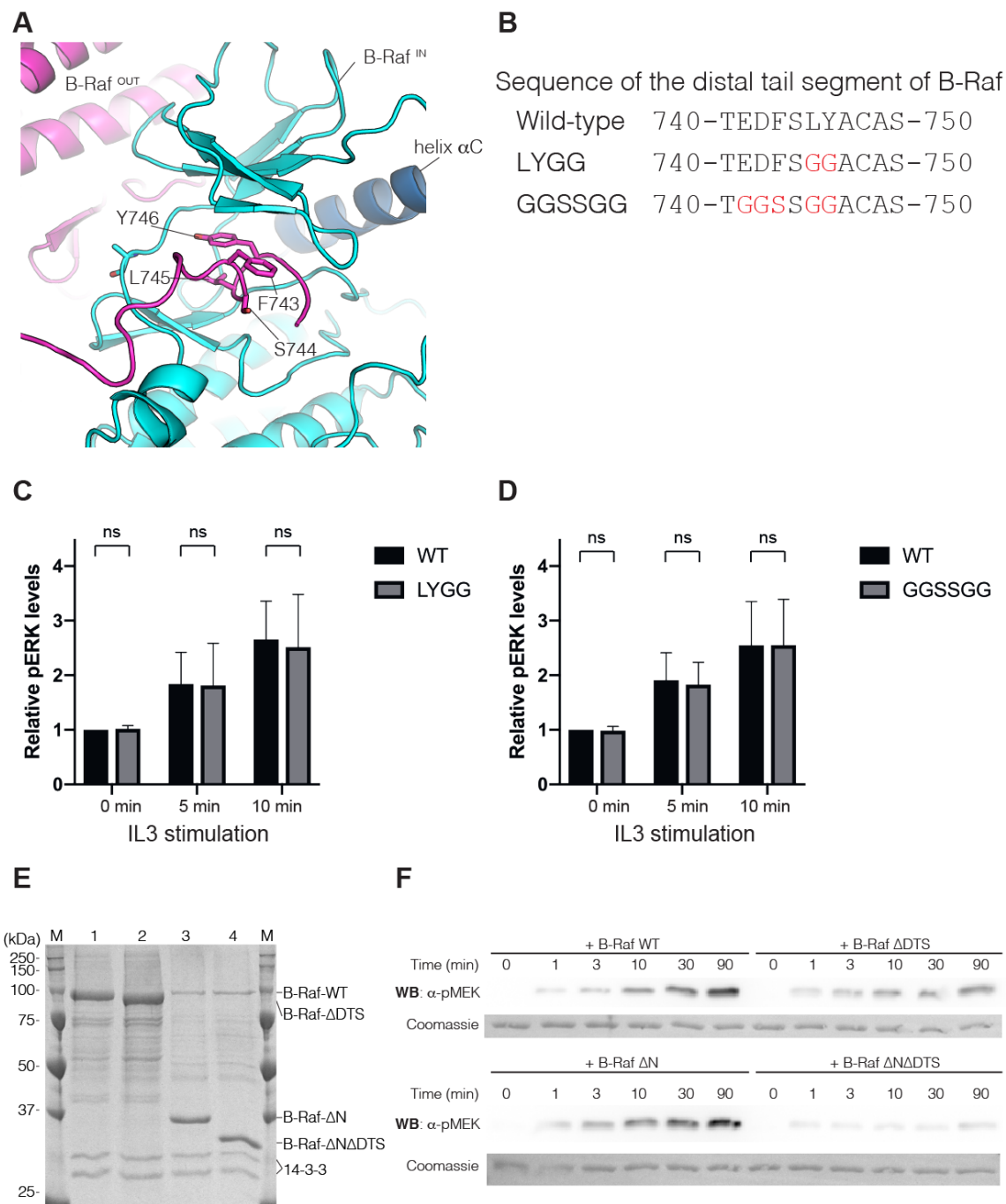


Fig. S11. Analysis of the effect of mutations in the distal tail segment of B-Raf. (A) Close-up view of active site of B-Raf^{IN} (cyan) with the distal tail segment of B-Raf^{OUT} (magenta). (B) Sequence of the portion of the B-Raf distal tail segment that interacts with the active site of B-Raf^{IN}. Two Raf variants, denoted LYGG and GGSSGG, correspond to changes in the sequence as shown. (C and D) Relative pERK levels for Ba/F3 cells expressing these B-Raf variants. Mean values for relative pERK levels and standard deviations were plotted from three flow cytometry experiments (the complete histograms for pERK levels in the experiments are shown in Fig. S9).

Mean relative pERK levels and their standard deviations were plotted by the same way as Fig. 3. No statistical significance was observed in this experiment, as indicated by ns (p value>0.05). (E and F) The result of the repeated experiment shown in Fig. 3H and I. (E) SDS-PAGE gel analysis of B-Raf constructs purified from HEK293T cells. M – Precision Plus Protein Unstained Standards (Bio-Rad); 1 – B-Raf-WT; 2 – B-Raf- Δ DTS; 3 – B-Raf- Δ N; 4 – B-Raf- Δ N Δ DTS. (F) Western blot analysis of MEK1 phosphorylation with the N-terminal regulatory region present and without the N-terminal regulatory region. Coomassie brilliant blue staining of the membrane shows the total amount of MEK1 protein loaded to each lane on the gel.

5

10

Figure S12.

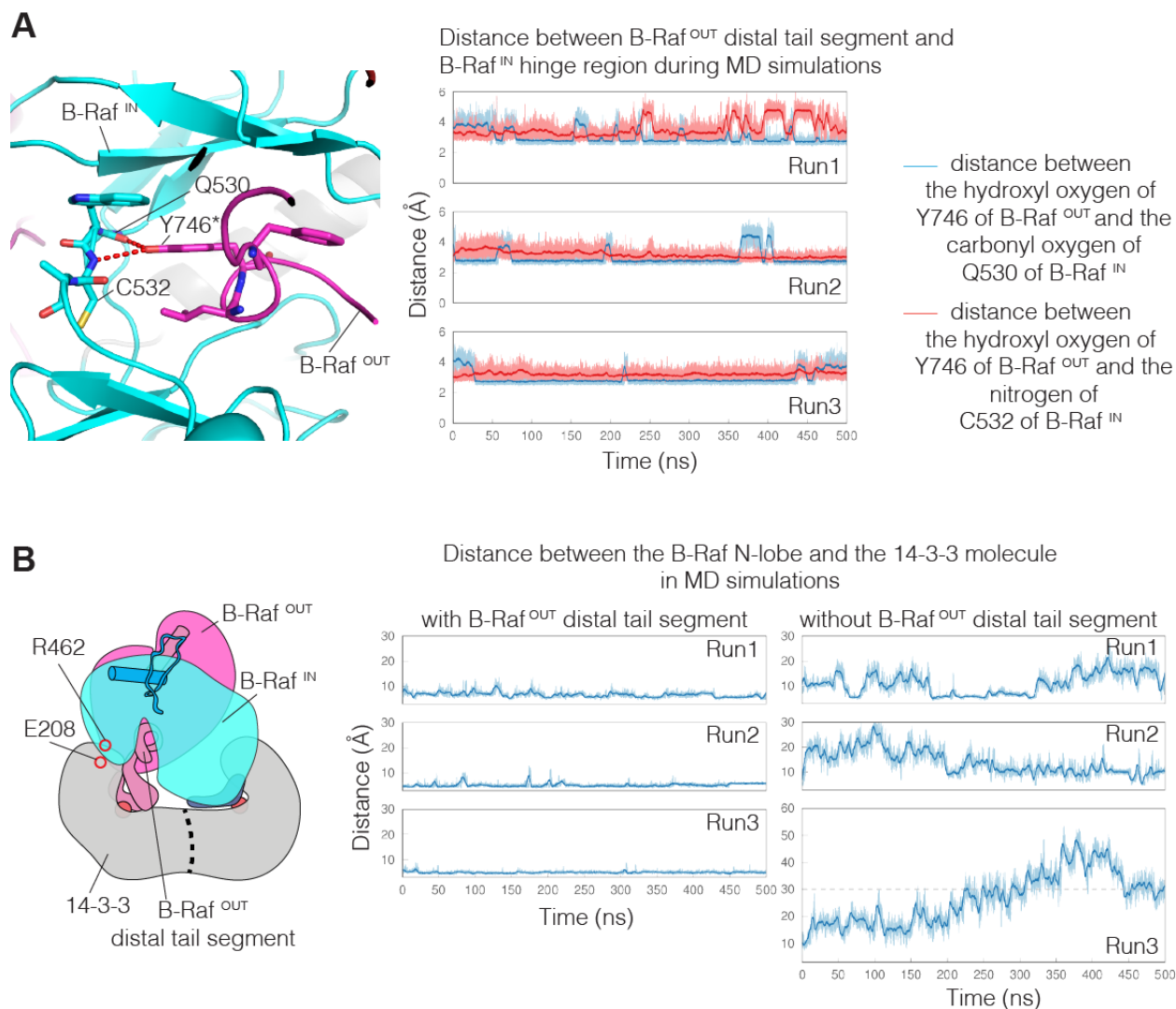


Fig. S12. Stability of the B-Raf:14-3-3 complex structure in molecular dynamics simulations.

(A) The structural diagram shows the active site of B-Raf^{IN} (cyan), with the distal tail segment of B-Raf^{OUT} (magenta). The hydroxyl group of Tyr⁷⁴⁶ makes two hydrogen bonds with the hinge connecting N- and C-lobes of the kinase (dotted lines). The graphs show the time evolution of the distance between the oxygen of the tyrosine sidechain and the carbonyl of Gln⁵³⁰ (cyan) and an amide nitrogen of Cys⁵³² (peach). In instantaneous structures sampled from the trajectories, at least one of the hydrogen bond is maintained. The darker traces are the time-averaged values of the distances calculated using a moving window of 4 ns. (B) Stability of the asymmetric conformation when the B-Raf^{OUT} distal tail segment present or absent. Time series of the distance between the C α atom of Arg⁴⁶², in the N-lobe of B-Raf^{IN} and the C α atom of Glu²⁰⁸ in 14-3-3. In the system with the distal tail segment present (left) the N-lobe of B-Raf^{IN} stays closely associated with 14-3-3, whereas in the system where the distal tail segment is absent (right), B-Raf^{IN} samples a range of conformations across the three simulations.

Figure S13.

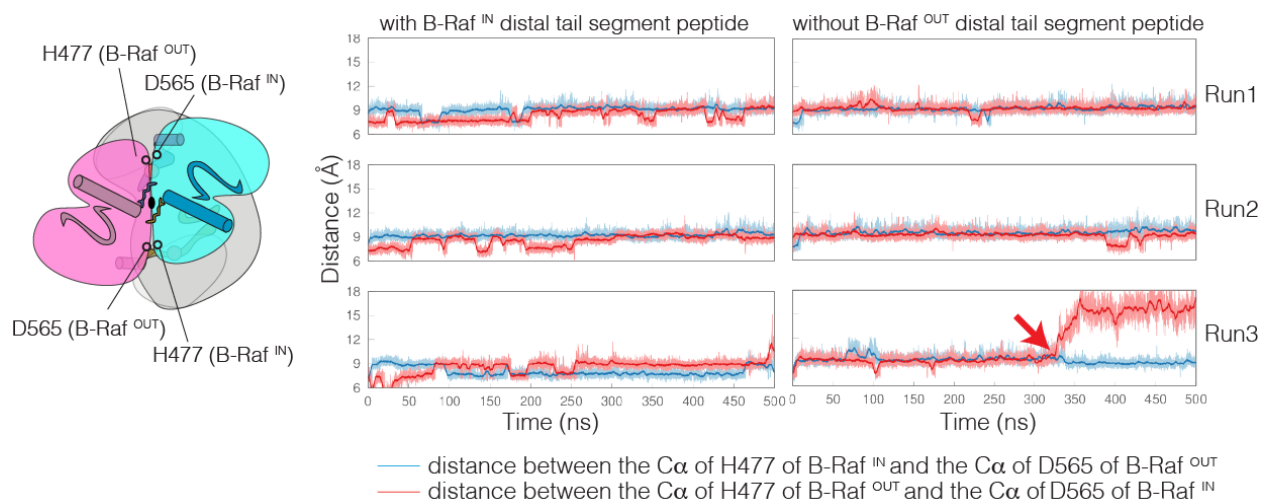


Fig. S13. Stability of the B-Raf dimer interface in molecular dynamics simulations. Distance between two B-Raf protomers are plotted during molecular dynamics simulations with or without B-Raf^{OUT} distal tail segment. The graphs show the time evolution of the distance between the Cα of His⁴⁷⁷ of B-Raf^{IN} and the Cα of Asp⁵⁶⁵ of B-Raf^{OUT} (cyan) and the distance between the Cα of His⁴⁷⁷ of B-Raf^{OUT} and the Cα of Asp⁵⁶⁵ of B-Raf^{IN} (peach). Red arrow indicates the breakage of the B-Raf dimer interface. The lighter shades are the actual distance and the darker curve represents the time-average of the distance, calculated with a period of 4 ns.

5

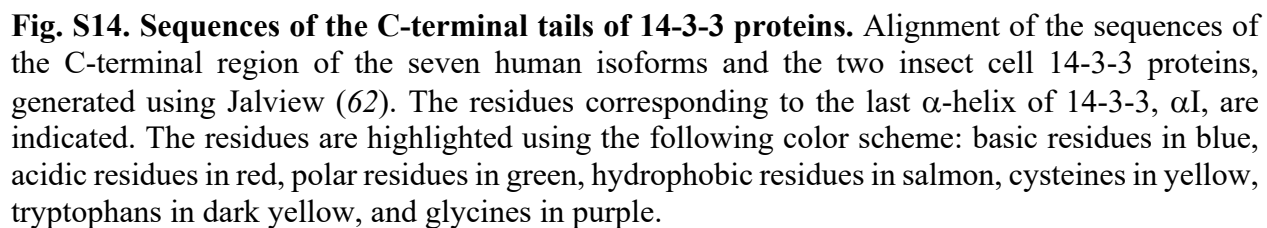


Figure S15.

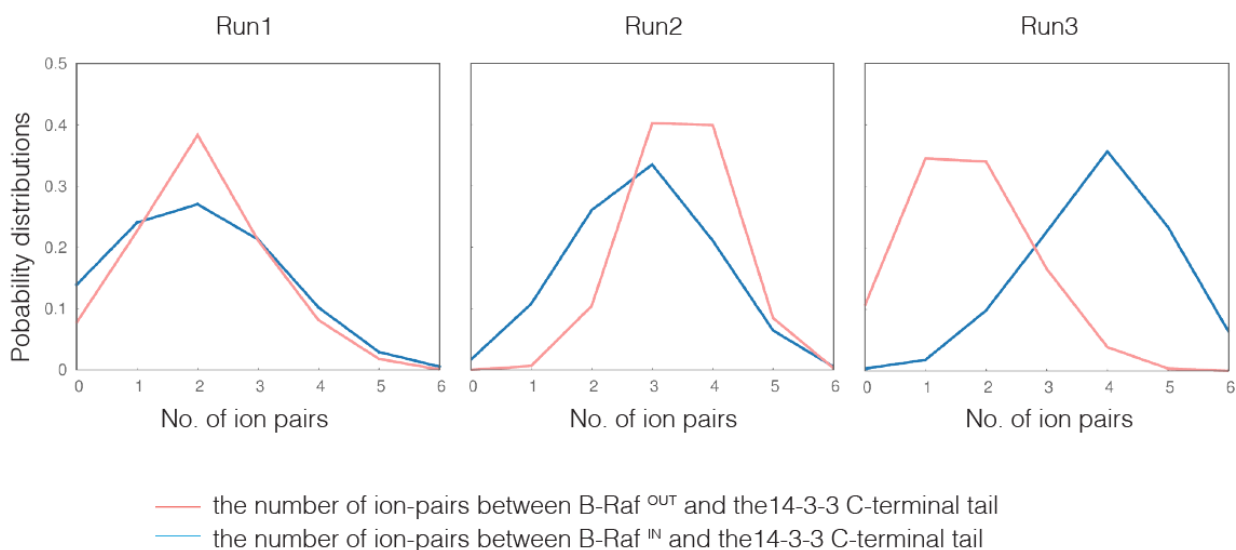


Fig. S15. The interaction between the B-Raf kinase domain and the 14-3-3 C-terminal tail.

B-Raf kinase domain presents positively charged surfaces near the C-terminal tails of 14-3-3, which contain multiple acidic residues (see Fig. S14). The number of ion pairs between B-Raf and the 14-3-3 C-terminal tail was counted during the simulations and shown as histograms.

Figure S16.

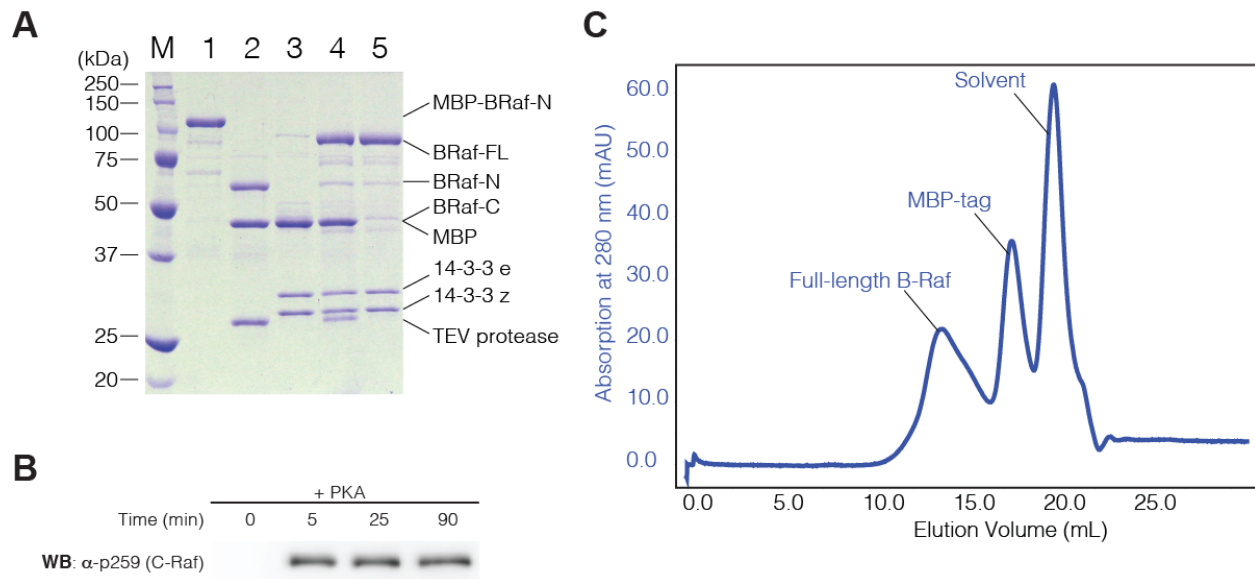


Fig. S16. SDS-PAGE gel analysis of the B-Raf samples. (A) Proteins produced during the production of B-Raf, analyzed by SDS-PAGE gel electrophoresis with Coomassie Brilliant Blue staining, showing the purification processes. M – Precision Plus Protein Unstained Standards (Bio-Rad); 1 - purified MBP-B-Raf-N fragment; 2 - MBP-B-Raf-N fragment after TEV protease treatment; 3 - purified B-Raf-C fragment; 4 - the product of intein reaction combining the B-Raf-N and B-Raf-C fragments; and 5 - purified full-length B-Raf. (B) Western blot analysis of the purified full-length B-Raf protein, the product of intein chemistry, with phospho-C-Raf (Ser²⁵⁹) antibody, which also detects B-Raf Ser³⁶⁵ phosphorylation (39). The purified B-Raf protein was incubated with PKA and ATP for indicated time at 30°C, and subsequently run on an SDS-PAGE gel. (C) Size exclusion chromatography profile of full-length B-Raf purification on Superose 6 column after intein reaction and TEV protease cleavage.

Figure S17.

A

human ϵ 1-255	1	-MDDREDLVYQAKLAEOAERYDEMVESMKKVAGMDV--ELTV EERNLLSV	47
insect ϵ 1-261	1	-MSEREDNVYKAKLAEOAERYDEMVEAMKNVASRNVSDNELTV EERNLLSV	50
human ζ 1-245	1	--MDKNELVQKAKLAEOAERYDMAACMKSVTEQGA--ELSN EERNLLSV	46
insect ζ 1-247	1	MSVDKEELVQRAKLAEOAERYDMAAAMKEVTETGV--ELSN EERNLLSV	48
human ϵ 1-255	48	AYKNVIGARRASWR I ISSIEQKEENKGGEDK LKM IREYRQMVETELKLC	98
insect ϵ 1-261	51	AYKNVIGARRASWR I ISSIEQKEETKGAEGK LNM IRAYRSQVEKELRDC	101
human ζ 1-245	47	AYKNVVGARRSSWRVVSSIEQKTE--GAEEKQQMAREYREK IETELRDC	95
insect ζ 1-247	49	AYKNVVGARRSSWRV I SSIEQKTE--GSEKQQMAREYRVKV EKELELRE	97
human ϵ 1-255	99	D ILDVLDKHLIP AANTGESKVFY YKMKGDYHRYLA EFATG NDRKEAAENSL	149
insect ϵ 1-261	102	D ILGVLDKHLIP SSQTGESKVFY YKMKGDYHRYLA EFATG NDRKEAAENSL	152
human ζ 1-245	96	DVLSLLEKFLIPNASQAESKVFY LKMKGDY YRYLA EVAAGDDKKG IVDQSQ	146
insect ζ 1-247	98	DV LGLLDKHLIP KASNPESKVFY LKMKGDY YRYLA EVAATGETRNSVVEDSQ	148
human ϵ 1-255	150	VAYKAA SDIAMTELPPTHPIRLGLALNFSVFYYEILNSPDRACRLAKAAFD	200
insect ϵ 1-261	153	VAYKAA SDIAMTELPPTHPIRLGLALNFSVFYYEILNSPDRACRLAKAAFD	203
human ζ 1-245	147	QAYQEA FEISKKEMQPTHPIRLGLALNFSVFYYEILNSPEKACSLAKTAFD	197
insect ζ 1-247	149	KAYQDA FEISKAKMQPTHPIRLGLALNFSVFYYEILNSPDKACQLAKQAFD	199
human ϵ 1-255	201	D AIAELDTLS EESYKDSTLIMQLLRDNLT LWTS DM QGDGEE---QNK EALQ	248
insect ϵ 1-261	204	D AIAELDTLS EESYKDSTLIMQLLRDNLT LWTS DM QGDGESGETEQKEQPQ	254
human ζ 1-245	198	E AIAELDTLS EESYKDSTLIMQLLRDNLT LWTS DT QGDFAE-----	238
insect ζ 1-247	200	D AIAELDTLN ED SYKDSTLIMQLLRDNLT LWTS DT QGDGDE-----	240
human ϵ 1-255	249	DV EDENQ	255
insect ϵ 1-261	255	DV EDQDV	261
human ζ 1-245	239	AGEGGEN	245
insect ζ 1-247	241	PAEGGDN	247

B

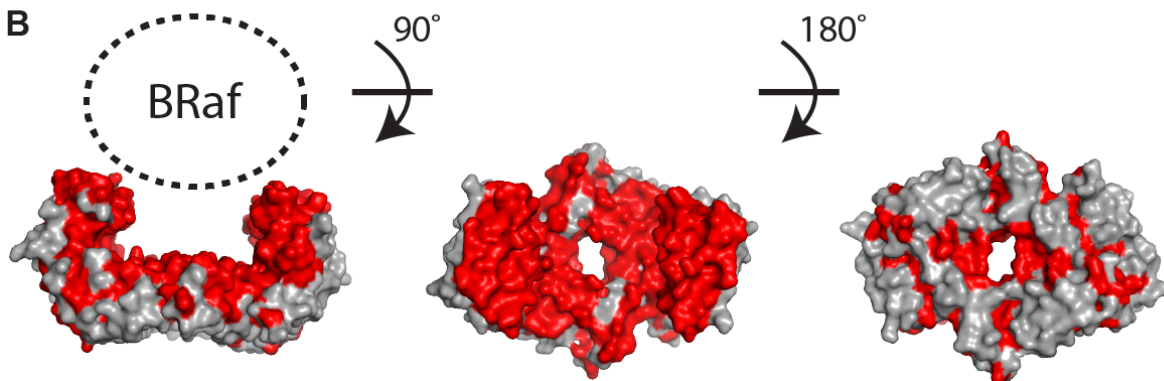


Fig. S17. Sequence conservation in 14-3-3 proteins. (A) Sequence alignment of human and insect 14-3-3 ϵ and ζ proteins. The conserved residues among all four genes are highlighted with red. (B) Mapping conserved residues on the 14-3-3 structure. Crystal structure of 14-3-3 σ in complex with the Raf C-terminal peptide (PDB ID: 4IEA) (47) is shown in surface representation. The residues conserved among human and *S. litura* 14-3-3 ϵ and ζ proteins are colored red and the others are gray. The position of the B-Raf dimer is indicated by dashed circle in the left panel.

Table S1. Phosphorylation sites of B-Raf identified by mass spectrometry

Phosphorylated residues	Peptide detected	Note
pT401	³⁸⁵ DQGFRGDGGSTTGLS t PPASLPGSLTNVK ⁴¹³ ³⁹⁰ GDGGSTTGLS t PPASLPGSLTNVK ⁴¹³	
pS419	⁴¹⁵ ALQK s PGPQR ⁴²⁴ ⁴¹⁹ s PGPQR ⁴²⁴	
pS429	⁴²⁷ K S SSSEDR ⁴³⁵	
pS447	⁴⁴⁴ RDS s DDWEIPDGQITVGQR ⁴⁶²	NtA motif
pS465	⁴⁶³ I G sGSFGTVYK ⁴⁷³	P-loop
pS602	⁶⁰² s RWSGSHQFEQLSGSILWMAPEVIR ⁶²⁶	Activation loop
pS614	⁶⁰⁴ WSGSHQFEQL s GSILWMAPEVIR ⁶²⁶	Activation loop
pS616	⁶⁰⁴ WSGSHQFEQLSG s ILWmAPEVIR ⁶²⁶	Activation loop
pS729	⁷²⁷ SA s EPSLNR ⁷³⁵	14-3-3 binding site
pS750	⁷³⁶ AGFQTEDFSLYAC s PK ⁷⁵²	
pT753	⁷⁵³ t PIQAGGYGAFPVH ⁷⁶⁶	

Phosphorylated residues are shown in bold lowercase.

Table S2. Statistics of B-Raf:14-3-3 complex structure determination

Data collection	
EM	Titan Krios 300kV, K2 Gatan Summit
Pixel size (Å)	0.532 (super-resolution mode)
Defocus range (μm)	-1.25 to -2.5
Micrographs	2,991
Reconstruction (RELION)	
Final micrographs	2,960
Final particles	113,313
Accuracy of rotations (°)	2.464
Accuracy of translations (pixel)	0.777
Final resolution (Å)	3.9
Map sharpening B factor (Å ²)	-126.1
Refinement (Phenix)	
Map:Model FSC _{0.5} (Å)	4.0
Map CC (mask)	0.79
Residue numbers	1007
Rms bond length (Å)	0.006
Rms bond angle (°)	0.96
Validation by Molprobit	
Geometry score (percentile)	1.87
Clash score (percentile)	7.55
Rotamer outliers (%)	0.77
Cβ outliers (%)	0.0
Ramachandran plot	
Favoured (%)	92.8
Allowed (%)	7.2
Outliers (%)	0.0

References

37. A. J. Stevens *et al.*, Design of a Split Intein with Exceptional Protein Splicing Activity. *J. Am. Chem. Soc.* **138**, 2162–2165 (2016).
- 5 38. S. K. Fetics *et al.*, Allosteric effects of the oncogenic RasQ61L mutant on Raf-RBD. *Structure*. **23**, 505–516 (2015).
39. A. Fischer *et al.*, Regulation of RAF activity by 14-3-3 proteins: RAF kinases associate functionally with both homo- and heterodimeric forms of 14-3-3 proteins. *J. Biol. Chem.* **284**, 3183–3194 (2009).
- 10 40. J. Zivanov *et al.*, New tools for automated high-resolution cryo-EM structure determination in RELION-3. *Elife*. **7** (2018), doi:10.7554/eLife.42166.
41. S. Q. Zheng *et al.*, MotionCor2: anisotropic correction of beam-induced motion for improved cryo-electron microscopy. *Nat. Methods*. **14**, 331–332 (2017).
- 15 42. A. Rohou, N. Grigorieff, CTFFIND4: Fast and accurate defocus estimation from electron micrographs. *J. Struct. Biol.* **192**, 216–221 (2015).
43. X. Bai, E. Rajendra, G. Yang, Y. Shi, S. H. W. Scheres, Sampling the conformational space of the catalytic subunit of human γ -secretase. *Elife*. **4**, e11182 (2015).
- 20 44. V. P. Stanton, D. W. Nichols, A. P. Laudano, G. M. Cooper, Definition of the human raf amino-terminal regulatory region by deletion mutagenesis. *Mol. Cell. Biol.* **9**, 639–647 (1989).
45. N. H. Tran, X. Wu, J. A. Frost, B-Raf and Raf-1 are regulated by distinct autoregulatory mechanisms. *J. Biol. Chem.* **280**, 16244–16253 (2005).
- 25 46. R. Kefford *et al.*, Phase I/II study of GSK2118436, a selective inhibitor of oncogenic mutant BRAF kinase, in patients with metastatic melanoma and other solid tumors. *J. Clin. Oncol.* **28**, 8503–8503 (2010).
47. M. Molzan *et al.*, Stabilization of physical RAF/14-3-3 interaction by cotylenin A as treatment strategy for RAS mutant cancers. *ACS Chem. Biol.* **8**, 1869–1875 (2013).
- 30 48. L. M. Stevers *et al.*, Characterization and small-molecule stabilization of the multisite tandem binding between 14-3-3 and the R domain of CFTR. *Proc. Natl. Acad. Sci. USA*. **113**, E1152-61 (2016).
49. P. Emsley, B. Lohkamp, W. G. Scott, K. Cowtan, Features and development of Coot. *Acta Crystallogr. Sect. D, Biol. Crystallogr.* **66**, 486–501 (2010).
50. P. D. Adams *et al.*, PHENIX: a comprehensive Python-based system for macromolecular structure solution. *Acta Crystallogr. Sect. D, Biol. Crystallogr.* **66**, 213–221 (2010).
- 35 51. T. D. Goddard *et al.*, UCSF ChimeraX: Meeting modern challenges in visualization and analysis. *Protein Sci.* **27**, 14–25 (2018).
52. J. Zheng *et al.*, 2.2 Å refined crystal structure of the catalytic subunit of cAMP-dependent protein kinase complexed with MnATP and a peptide inhibitor. *Acta Crystallogr. Sect. D, Biol. Crystallogr.* **49**, 362–365 (1993).

53. W. L. Jorgensen, J. Chandrasekhar, J. D. Madura, R. W. Impey, M. L. Klein, Comparison of simple potential functions for simulating liquid water. *J. Chem. Phys.* **79**, 926 (1983).
54. W. Humphrey, A. Dalke, K. Schulten, VMD – Visual Molecular Dynamics. *J. of Mol. Graph.* **14**, 33–38 (1996).
- 5 55. J. C. Phillips *et al.*, Scalable molecular dynamics with NAMD. *J. Comput. Chem.* **26**, 1781–1802 (2005).
56. J. Huang *et al.*, CHARMM36m: an improved force field for folded and intrinsically disordered proteins. *Nat. Methods.* **14**, 71–73 (2017).
- 10 57. T. Darden, D. York, L. Pedersen, Particle mesh Ewald: An $N \cdot \log(N)$ method for Ewald sums in large systems. *J. Chem. Phys.* **98**, 10089 (1993).
58. G. J. Martyna, D. J. Tobias, M. L. Klein, Constant pressure molecular dynamics algorithms. *J. Chem. Phys.* **101**, 4177 (1994).
59. S. E. Feller, Y. Zhang, R. W. Pastor, B. R. Brooks, Constant pressure molecular dynamics simulation: The Langevin piston method. *J. Chem. Phys.* **103**, 4613–4621 (1995).
- 15 60. D. A. Case *et al.*, The Amber biomolecular simulation programs. *J. Comput. Chem.* **26**, 1668–1688 (2005).
61. E. F. Pettersen *et al.*, UCSF Chimera—a visualization system for exploratory research and analysis. *J. Comput. Chem.* **25**, 1605–1612 (2004).
- 20 62. A. M. Waterhouse, J. B. Procter, D. M. A. Martin, M. Clamp, G. J. Barton, Jalview Version 2--a multiple sequence alignment editor and analysis workbench. *Bioinformatics.* **25**, 1189–1191 (2009).